Electronic Supplementary Material (ESI) for Green Chemistry.

Supporting Information for

Efficient Hydrogenation Catalytic Model Hosted in Stable Hyper-crosslinked Porous-Organic-Polymer: From Fatty Acids to Bio-based Alkanes Diesel Synthesis

Chitra Sarkar,[#,a] Subhash Chandra Shit,[#,a] Duy Quang Dao,[#,b] Jihyeon Lee,[c] Ngoc Han Tran,[d] Ramana Singuru,[a] Kwangjin An,[c] Nguyen Dang Nam,[b] Quyet Van Le,[b] Prince Nana Amaniampong,[e] Asmaa Drif,[f] Francois Jerome,[e,f] Pham Thanh Huyen,[g] Thi To Nga Phan,[g] Dai-Viet N. Vo,[h] Nguyen Thanh Binh,[i] Quang Thang Trinh*,[b,j] Matthew P. Sherburne*,[k,l] and John Mondal*,[a]

[a] *Catalysis & Fine Chemicals Division, CSIR-Indian Institute of Chemical Technology, Uppal Road, Hyderabad-500007, India.*

[b] *Institute of Research and Development, Duy Tan University, 03 Quang Trung, Danang 550000, Viet Nam.*

[c] *School of Energy & Chemical Engineering, Ulsan National Institute of Science and Technology (UNIST), Ulsan 689-798, Korea.*

[d] *Department of Aquatic Sciences and Assessment, Swedish University of Agricultural Sciences SLU, Box 7050, SE-750 07 Uppsala, Sweden.*

[e] *CNRS Research federation INCREASE, 1 rue Marcel Doré, TSA 41105, 86073 Poitiers, France.*

[f] *Institut de Chimie des Milieux et Matériaux de Poitiers (IC2MP), Université de Poitiers, CNRS, 1 rue Marcel Doré, TSA 41105, 86073 Poitiers, France.*

[g] *School of Chemical Engineering, Hanoi University of Science and Technology, 1 Dai Co Viet, Hanoi, Viet Nam.*

[h] *Center of Excellence for Green Energy and Environmental Nanomaterials (CE@GrEEN), Nguyen Tat Thanh University, 300A Nguyen Tat Thanh, District 4, Ho Chi Minh City 755414, Vietnam.*

[i] *Faculty of Chemistry, Hanoi University of Science, Vietnam National University (VNU), 19 Le Thanh Tong, Hanoi, Vietnam.*

[j] *Cambridge Centre for Advanced Research and Education in Singapore (CARES), 1 Create Way, 138602 Singapore.*

[k] *Berkeley Educational Alliance for Research in Singapore (BEARS), 1 CREATE Way, 138602 Singapore.*

[l] *Materials Science and Engineering Department, University of California, Berkeley, California 94720, United States.*

[#] These authors have equally contributed in this manuscript.

Corresponding authors:

*Email: qttrinh@ntu.edu.sg; trinhquangthang@duytan.edu.vn (Q.T.T);

mpsherb@berkeley.edu (M.P.S);

johncuchem@gmail.com; johnmondal@iict.res.in (J.M)

1. Characterization Techniques and Experimental Results:

Wide angle Powder X-ray diffraction (PXRD) patterns for samples were recorded with a Bruker D8 Advance X-ray diffractometer operated at a voltage of 40 kV and a current of 40 mA using Ni-filtered Cu Kα (λ =0.15406 nm) radiation. High-resolution transmission electron microscopy (HR-TEM) images were recorded in a JEOL JEM 2010 transmission electron microscope with operating voltage 200 kV equipped with a FEG. Field emission scanning electron microscopic images of samples were obtained using a JEOL JEM 6700 field emission scanning electron microscope (FESEM). HAADF-STEM measurements were carried out with a modified FEI Titan microscope (TEAM0.5) operated at 300 KV with a HAADF detector. The STEM probe semi-angle is 30 mrad, at a spatial resolution of 0.05 nm. EELS were acquired with a Nion U-HERMS200 microscope operated at 60 kV. Nitrogen adsorption isotherms were obtained using a Quantachrome Autosorb 1C surface area analyzer at 77 K. Prior to the measurement, the samples were degassed at 413 K for approximately 6 h in high vacuum. Surface areas were calculated from the adsorption data using Brunauer-Emmett-Teller (BET) in the relative pressure (P/P_0) range of 0.01-0.1. The total pore volumes and pore size distribution curves were obtained from the adsorption branches using nonlocal density functional theory (NLDFT) method. FT-IR spectra of the samples were recorded using a Nicolet MAGNA-FT IR 750 spectrometer Series II. Thermogravimetry (TGA) analyses of the sample were carried out using a TGA Instruments thermal analyzer TA-SDT Q-600. Solid-state 13C CP-MAS NMR studies were performed using a Bruker Avance III HD 400 MHz NMR spectrometer. X-ray photoelectron spectroscopy (XPS) was performed on an Omicron-NanoTechnology instrument operated at 15 kV and 20 mA with a monochromatic Al Kα X-ray source. A quadrupole ion trap mass spectrometer equipped with a Thermo Accela LC and an Agilent 6890 GC system equipped with a flame ionization detector were used for analysis of catalytic reactions. The loading amount of Pd was determined using an inductively coupled plasma mass spectrometer (ICP-MS, X Series II, Thermo Scientific).

Synthesis of Pd@PPN-1: In a typical synthesis procedure, polymer PPN (0.200 g) was dispersed in methanol (40 mL) by sonication.[1] Then $Pd(OAc)_2$ (0.04 g) was added in the solution, and the resulting mixture was allowed to reflux at 65 °C under N_2 atmosphere for 8 h. After that the black solid material was isolated by simple filtration and washed with methanol 2-3 times. Then, the black material was dried in air and designated as Pd@PPN-1.

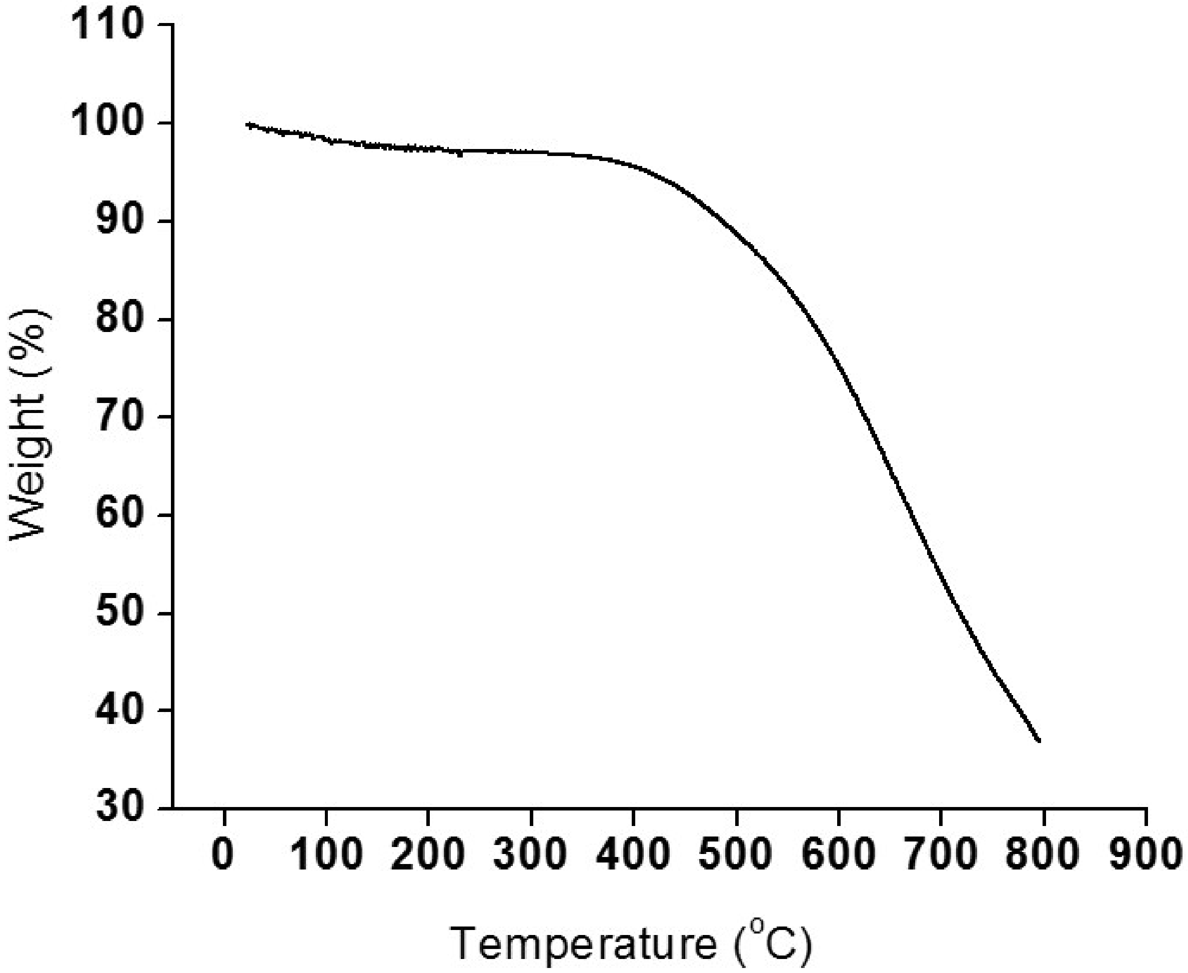

Figure S1: Thermogravimetric analysis (TGA) data of as-synthesized PPN.

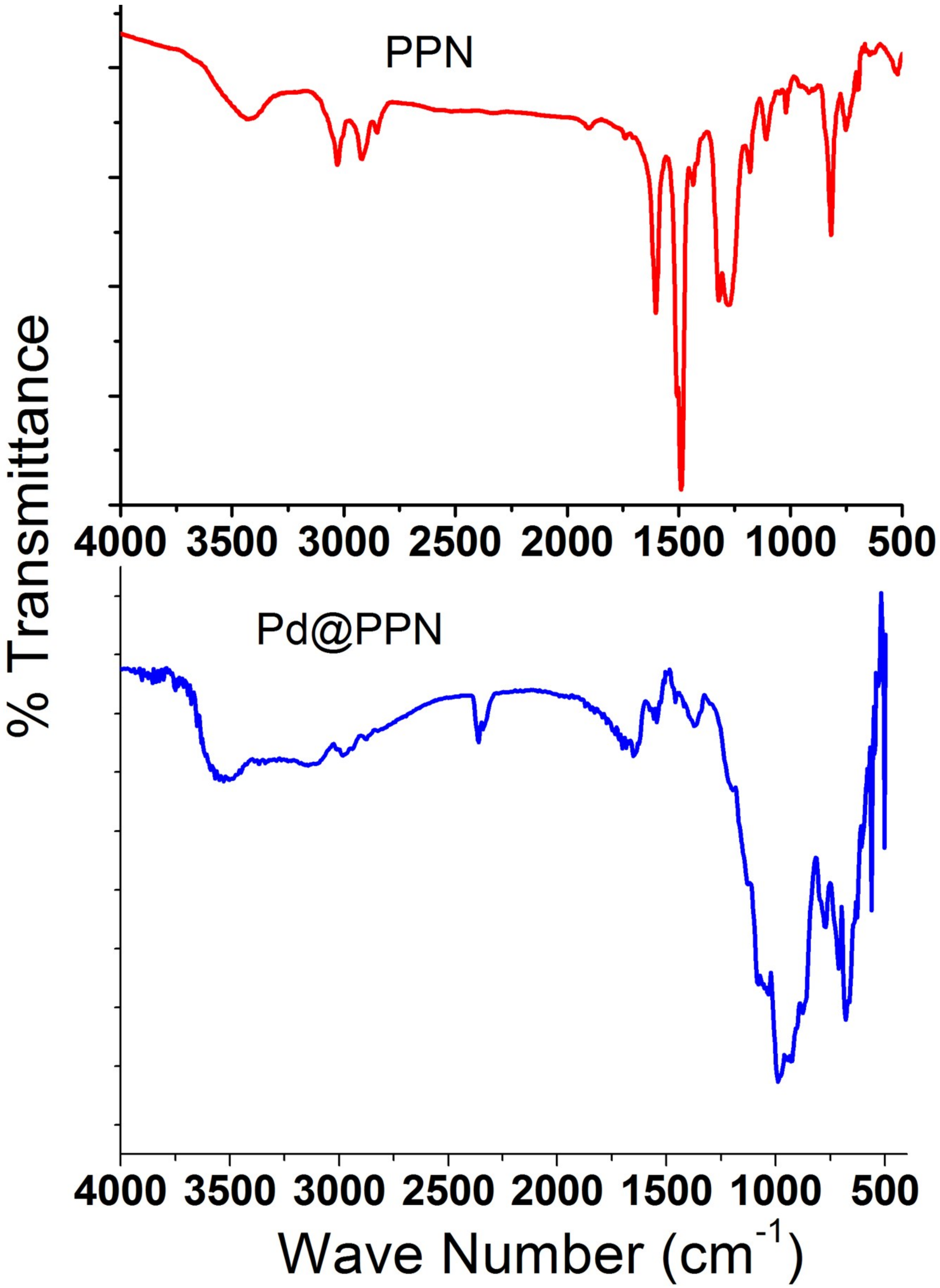

Figure S2: Fourier transformed infrared (FT-IR) spectra of as-synthesized PPN & Pd@PPN.

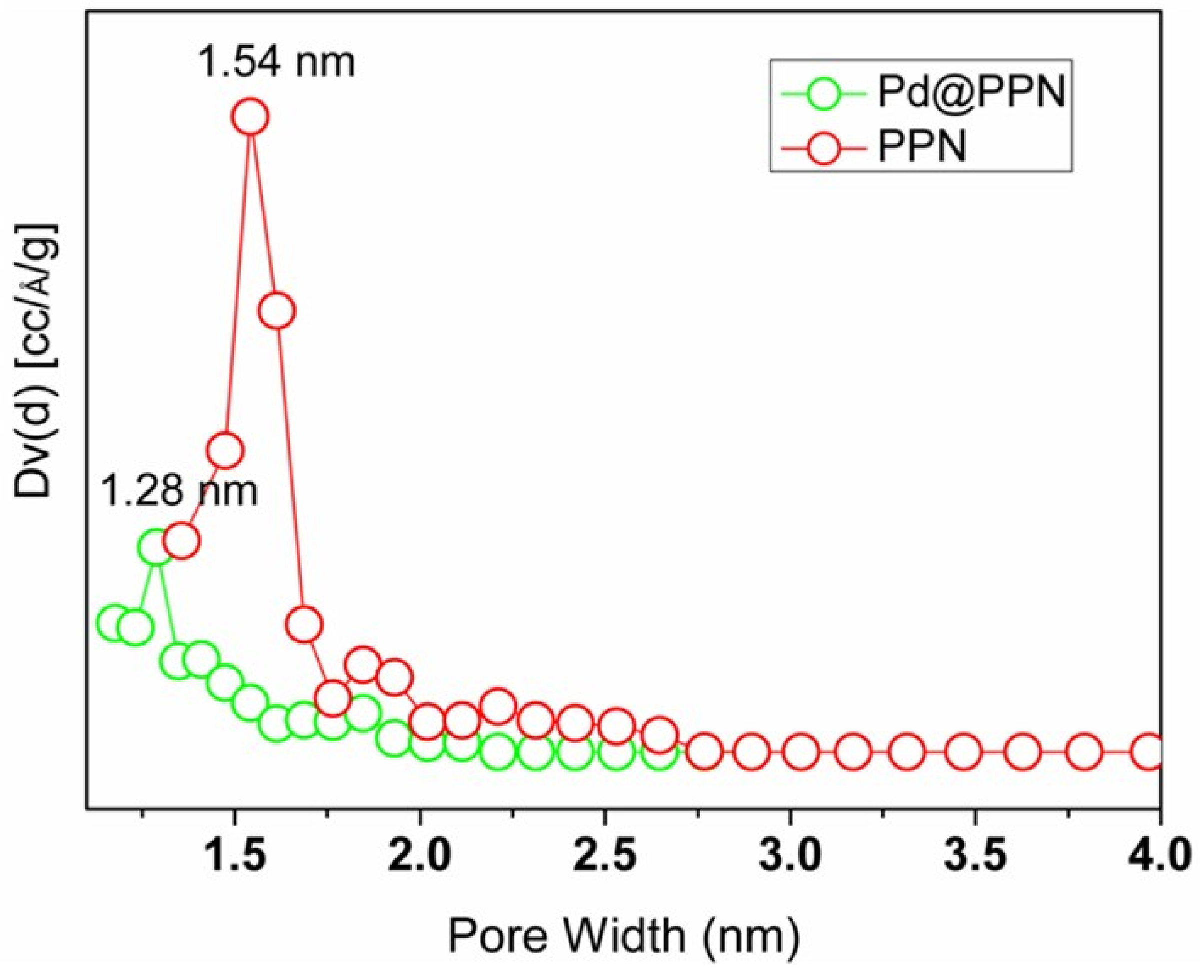

Figure S3: Pore-size distributions of the corresponding PPN and Pd@PPN materials, respectively, as measured by employing NLDFT (Non-Local-Density-Functional-Theory) method.

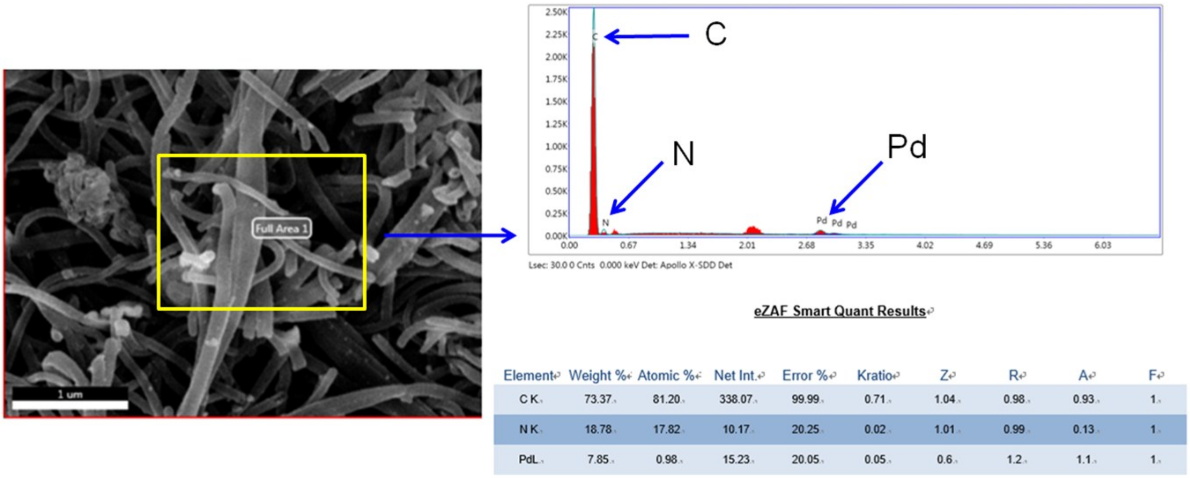

eZAF Smart Quant Results

Element	Weight %	Atomic %	Net Int.	Error %	Kratio	Z	R	A	F
C K	73.37	81.20	338.07	99.99	0.71	1.04	0.98	0.93	1
N K	18.78	17.82	10.17	20.25	0.02	1.01	0.99	0.13	1
PdL	7.85	0.98	15.23	20.05	0.05	0.6	1.2	1.1	1

Figure S4: Representative FE-SEM image of Pd@PPN in the particular selected area consists of spectra (marked with yellow box) and the corresponding Energy dispersive X-ray (EDX) spectrum for elemental distributions.

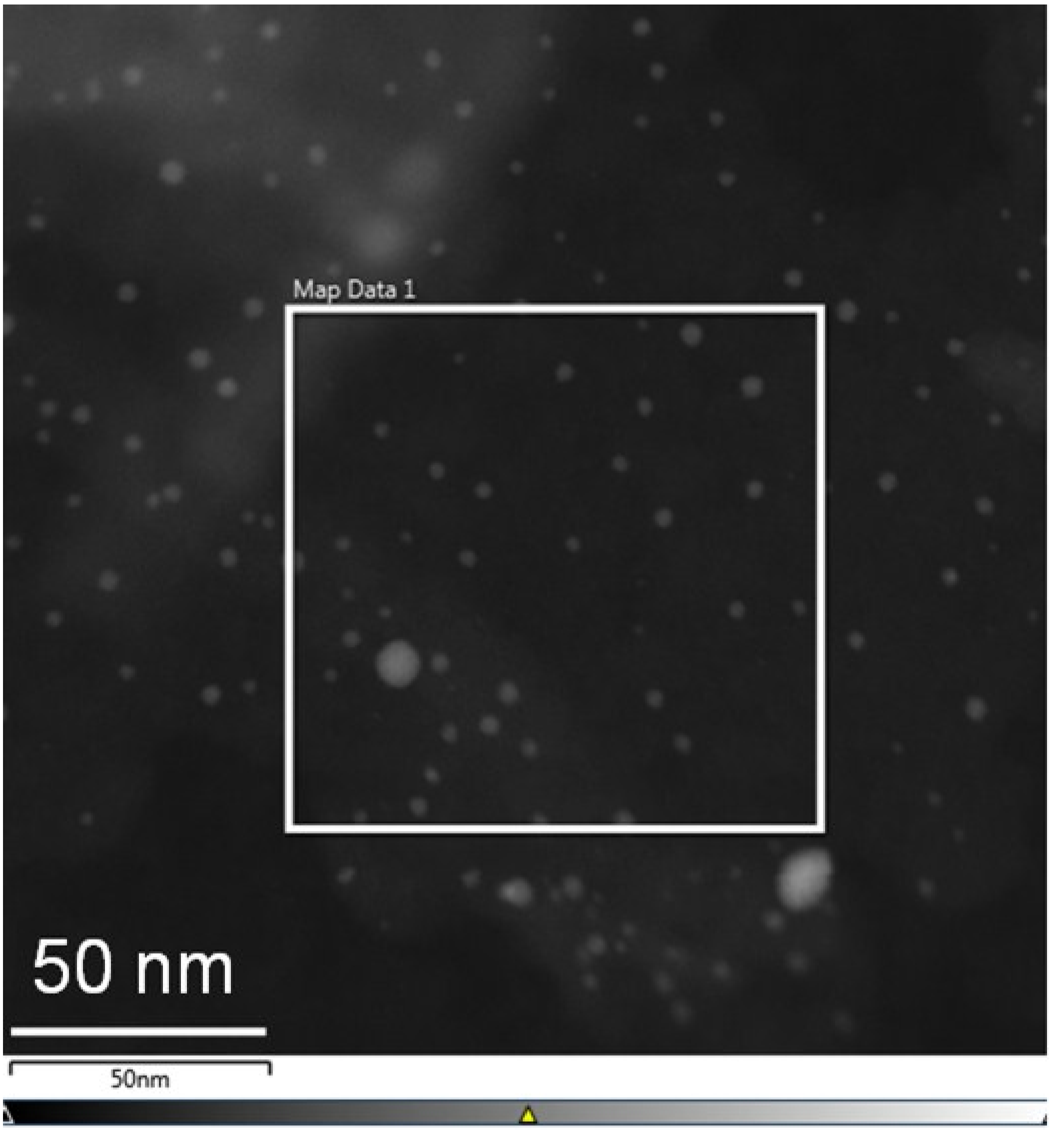

Figure S5: Representative high angle annular dark field scanning transmission electron microscopy (HAADF-STEM) image of Pd@PPN.

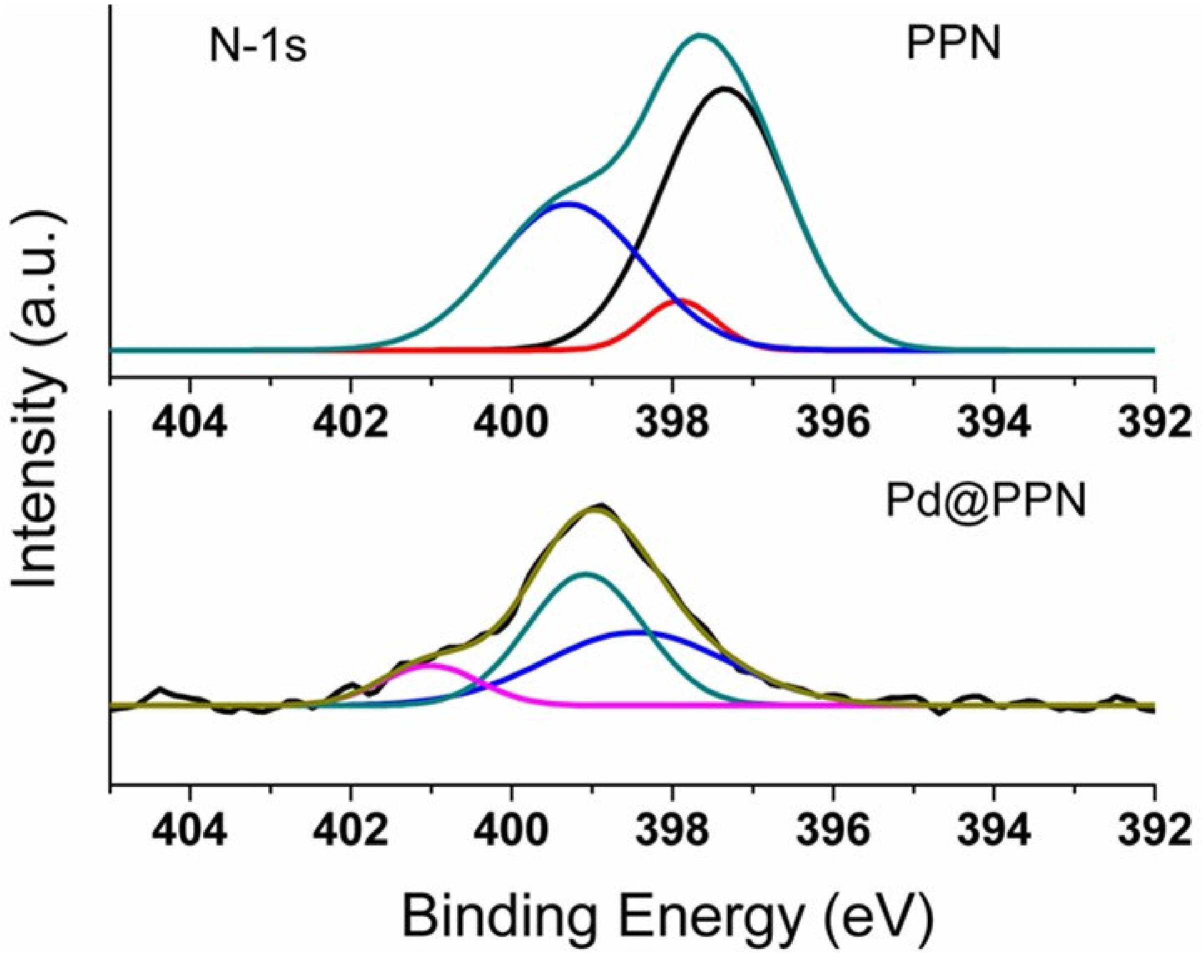

Figure S6: Fitted X-ray photoelectron spectra for the N-1s core-region of as-synthesized PPN and Pd@PPN, respectively.

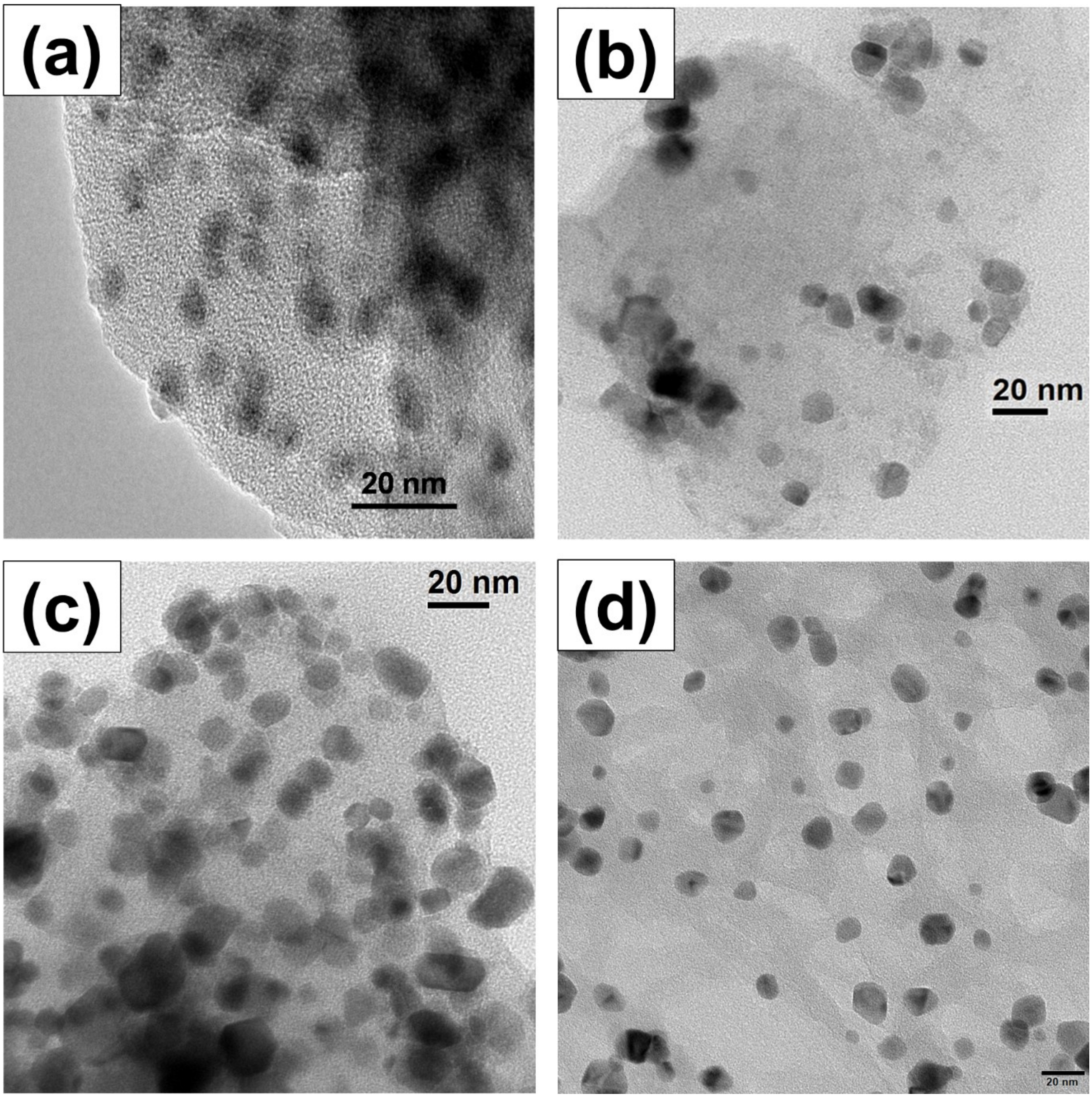

Figure S7. TEM images for catalysts in Table 1 of the main text: (a) Pd/C (size ~9.5 nm); (b) Pd/ZrO_2 (size ~19.2 nm); (c) Pd/TiO_2 (size ~15.3 nm); (b) Pd@PPN-1 (size ~8.9 nm);

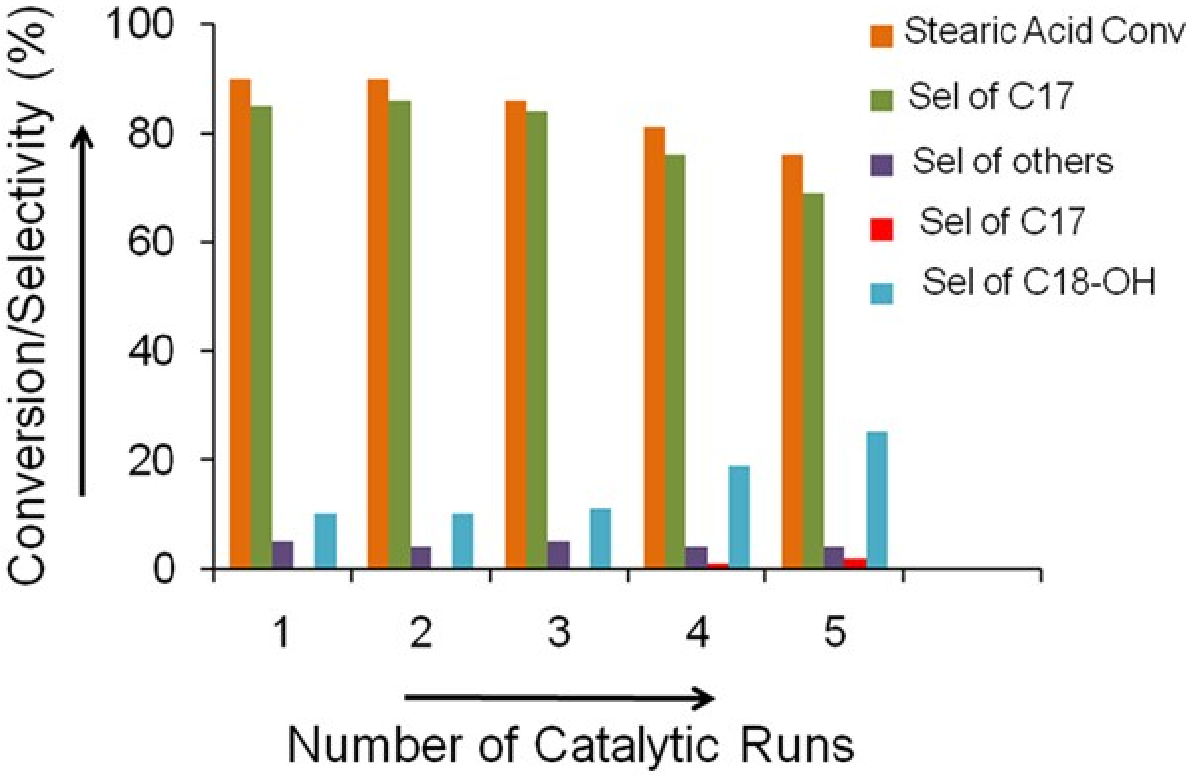

Figure S8: Recycling efficiency of Pd@PPN catalyst on the hydrogenation of stearic acid under optimized reaction conditions. Reaction conditions: Stearic acid (500 mg, 1.75 mmol), Pd-Catalyst (100 mg), 150°C, H_2 pressure (30 bar), Time (12 h), 350 mL of water in 1000 mL stainless steel autoclave.

Table T1: Effects of Impurities addition in the Stearic acid hydrogenation over Pd@PPN Catalyst

Entry	**Impurity addition**	**Conversion (%)**	**Alkanes Selectivity (%)**	**Others (%)**
1	NaCl	93.9	87.6	6.3
2	Glucose	94.5	85.8	8.7
3	Histidine	46.8	29.3	17.5
4	Acetic acid	82.9	69.4	13.5
5	Butyl amine	38.7	14.4	24.3
6	Cellulose	92.4	83.4	9.0

Reaction conditions: Stearic acid (100 mg, 0.350 mmol), Pd-Catalyst (20 mg, 2.6 mol% of Pd feed), 150°C, H_2 pressure (30 bar), Time (12 h) in 70 mL of water, 0.2 mmol of each compound was added. The designation "others" denotes cracking products, corresponding alcohol, and esters.

A series of stearic acid hydrogenation catalysed by Pd@PPN under optimized conditions were performed with the addition of different impurities (Table T1). Upon addition of NaCl, Pd@PPN catalyst afforded 93.9% stearic acid conversion (entry 1, Table T1), revealing that inorganic salt did not inhibit the hydrogenation reaction. The presence of NaCl as Na^+ and Cl^- ions effectively promoted the fatty acid ionization, thereby facilitating the interaction between catalyst surface and fatty acid. No significant effect is noticed on glucose addition (entry 2, Table T1). The use of histidine (pH =7.59) (entry 3, Table T1) where the extra imidazole N-atom of amino acid combined with the fatty acid and thus resulting reaction progress sluggish in nature.[2] We found strong influence on addition of acetic acid in the reaction medium with the a good conversion in comparison with the histidine (entry 4, Table T1). The addition of butyl amine as impurity drastically retarded the reaction improvement (entry 5, Table T1), due to the formation of amide linkage. In contrast, cellulose addition gave no difference to the original reaction (entry 6, Table T1).

Table T2: Fatty acids compositions of various vegetable oils

Vegetable Oils	Myristic acid (C14:0)	Palmitic acid (C16:0)	Stearic acid (C18:0)	Oleic acid (C18:1)	Linoleic acid (C18:2)	Linolenic acid (C18:3)
	Fatty acids/wt%					
Palm Oil	2.0	43.6	4.5	41.8	8.1	0
Soyabean Oil	0	11.8	3.8	22.7	54.2	7.4
Sunflower Oil	0	6.3	5.6	24.3	64.4	8.4
Rapeseed Oil	0	5.8	2.3	58.5	25.2	0

2. Electronics properties of Pd_{23} cluster interacting with PPN materials.

The interaction between a PPN monomer model with Pd cluster constituted of 23 atoms (Pd_{23}) were investigated in this work to fully evaluate the electronic properties of Pd_{23}@PPN molecular system, the charge transfer and electronic orbital interactions. All calculations were performed using Gaussian 16 A.03 package.[3] In this work, we employed hybrid density functional B3LYP[4, 5] in combination with the LANL2DZ (Los Alamos National Laboratory 2 double-ζ) basis set[6], which has been a widely used effective core potential (ECP)-type basis set for modelling the systems including transition metal atoms like Pd. We also took into account the empirical dispersion by using Grimme's D3 corrections for all the calculations.[7] This computational approach has been widely used to model Pd clusters as well as the interaction between different Pd clusters with organic compounds containing C, H and O elements. Bertani *et al.* used the B3LYP/LANL2DZ level of theory to calculate the interaction of Pd_n (n=2−7) with CH_x species (x=0−3), and this approach provided the best fit with experimental data.[8] For example, the calculated bond strength of Pd−Pd bond was reported of 22.1 kcal.mol^{-1} and the one of Pd−H bond was 57.7 kcal.mol^{-1}, while the experimental data was of 23.9 ± 3.6 and 55.9 ± 6 kcal.mol^{-1}, respectively. Zanti and Peeters also used the B3LYP/Lanl2DZ level to study the interaction of Pd_n (n = 2–9) with CO.[9] The authors reported the high accuracy of this method in reproducing the Pd−Pd bond length (experimental data being of 2.4 – 2.5 Å *vs*. calculated one of 2.53 Å) and the binding energy ΔE_B (experimental data of 1.03 ± 0.16 eV *vs.* calculated one being 0.96 eV). Moreover, Xing *et al.* also reported the reliability of the B3LYP/LANL2DZ method in the modelling of Pd_n (n = 2–20) cluster in both charged and neutral forms.[10] The authors showed that the detachment energies are in good agreement with the experimental data. For the binding energy (E_b), which is related to the stability of the cluster, it is showed that the Pd cluster becomes more stable as function of the cluster size up to 20 atoms. The same observations were also reported by Zanti and Peeters,[9] and Rogan *et al.,*[11] for Pd_n (n = 1−10) and Pd_n (n = 14−21) clusters, respectively. We chose the size of Pd cluster consisting of 23 atoms as proposed by Nava *et al.*[12] to ensure the stability of the Pd cluster during the interaction with PPN monomer. Moreover, electronic properties, charge transfer and orbitals interaction of the Pd_{23}@PPN were analysed by means of frontier orbitals (HOMO – highest orbital molecular orbital and LUMO – lowest unoccupied molecular orbital), natural bond orbital (NBO) analysis,[13] electrostatic potential (ESP) maps and by calculating natural population analysis (NPA) charge.

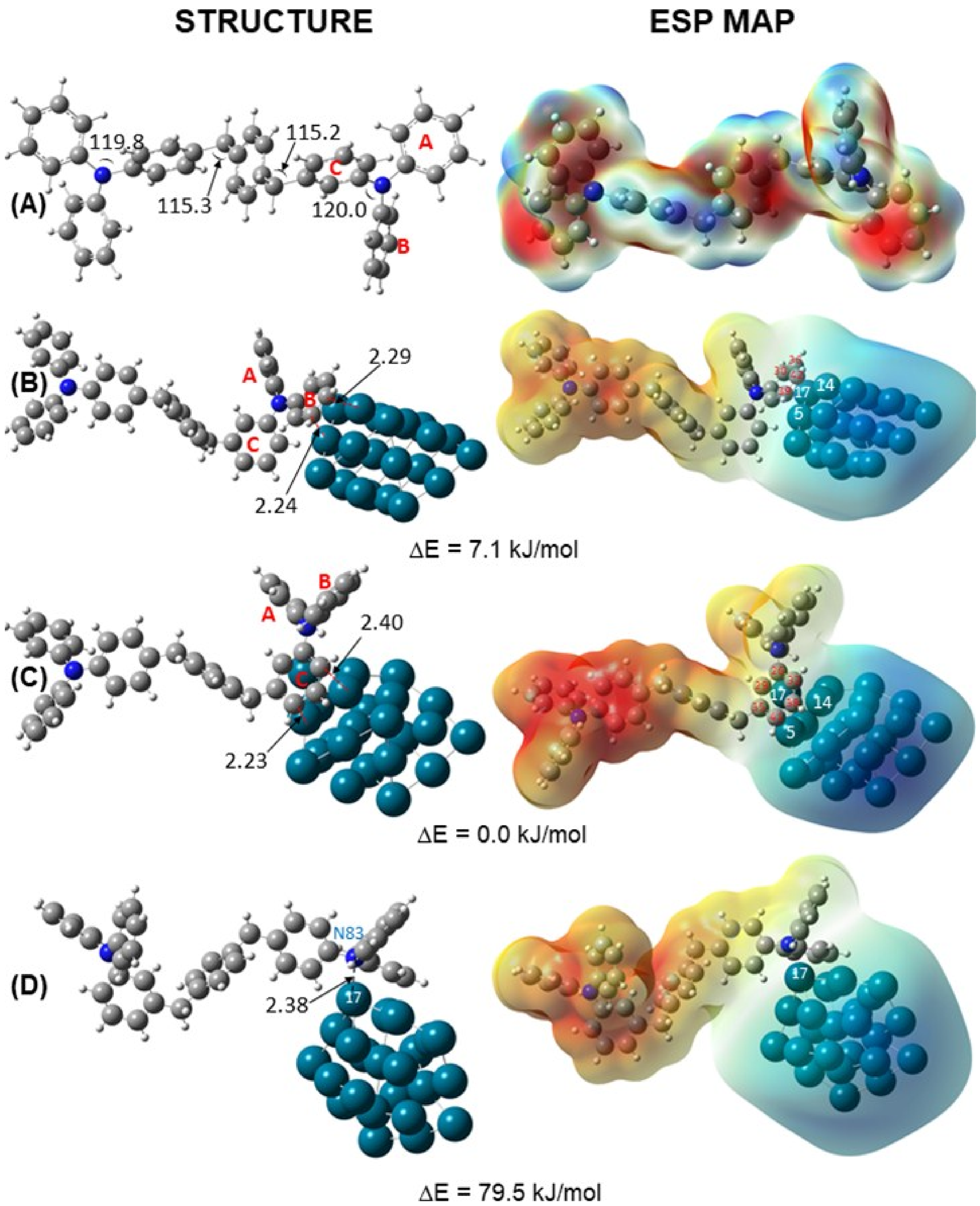

Figure S9: Optimized structures and electrostatic potential (ESP) maps for (**A**) PPN monomer; and different interacting configurations: (**B**) Ring B of PPN monomer interacting with one surface of Pd_{23} cluster (PPN-ring B@Pd_{23}-surface); (**C**) Ring C of PPN monomer interacting with one surface of Pd_{23} cluster (PPN-ring C@Pd_{23}-surface); (**D**) N83 atom of PPN monomer interacting with one atom on top of Pd_{23} cluster (PPN-N83@Pd_{23}-top). (ΔE indicates relative enthalpy of each configuration compared to the most stable one. Angles are in degree. Bond lengths are in Å).

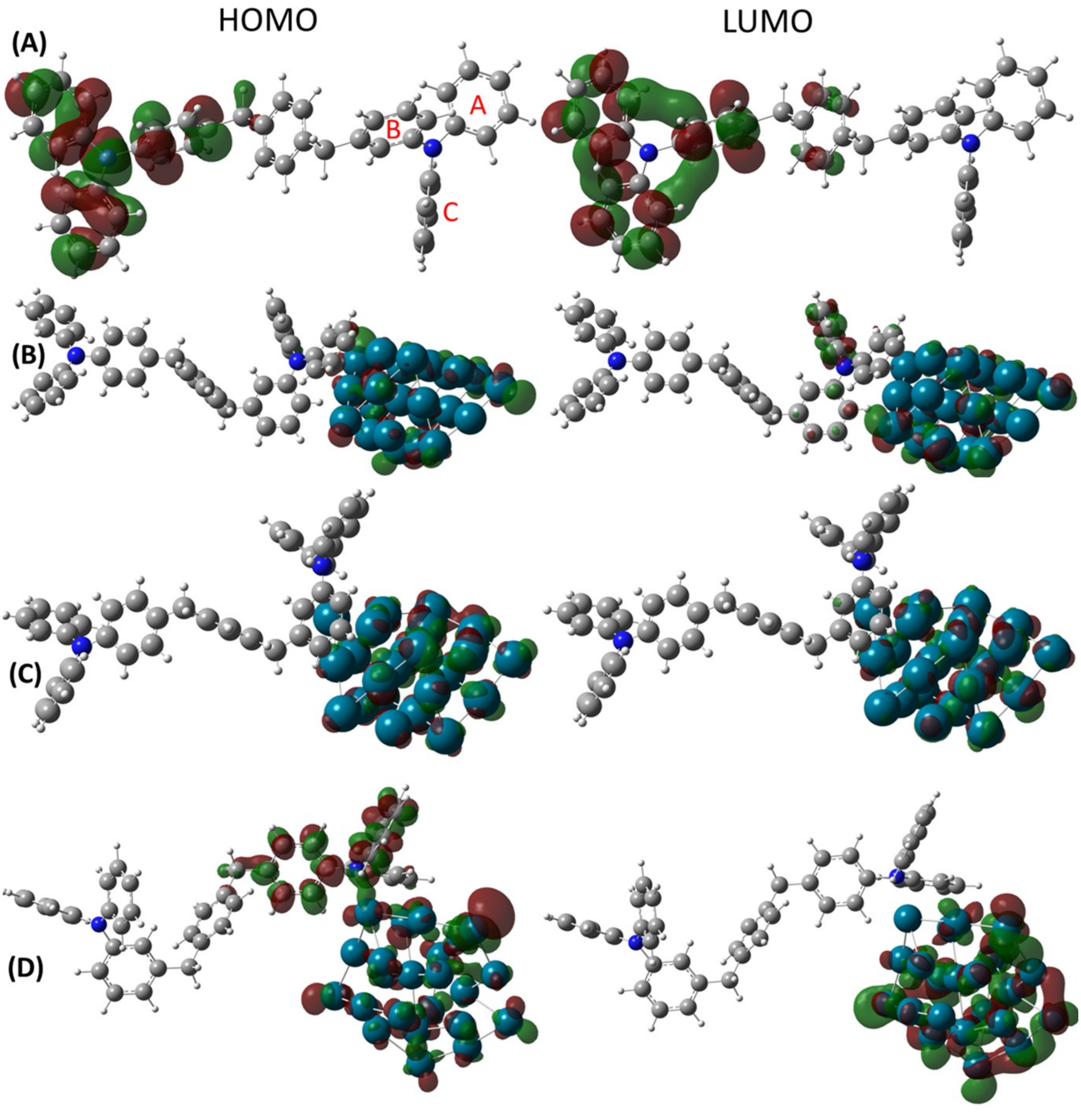

Figure S10: HOMO and LUMO distributions for different interaction configurations: (**A**) PPN monomer; (**B**) Ring B of PPN monomer interacting with one surface of Pd_{23} cluster (PPN-ring B @ Pd_{23}-surface); (**C**) Ring C of PPN monomer interacting with one surface of Pd_{23} cluster (PPN-ring C @ Pd_{23}-surface); (**D**) Two rings A and B of PPN monomer interacting with two surfaces of Pd_{23} cluster (PPN-2rings @ Pd_{23}-2sufaces) and (**E**) N83 atom of PPN monomer interacting with one atom on top of Pd_{23} cluster (PPN-N83 @ Pd_{23}-top)

Table T3: Enthalpies (E, hartree), relative enthalpies (ΔE, kJ/mol) and binding energies ($E_{binding}$, kJ/mol) of four interaction modes between PPN and Pd_{23} cluster

Interaction modes	**E, (hartree)**	**ΔE, kJ/mol**	**$E_{binding}$, (kJ/mol)**
PPN-ring B@Pd_{23}-surface	-4722.5762	7.1	125.5
PPN-ring C@Pd_{23}-surface	-4722.5789	0.0	132.2
PPN-2rings@Pd_{23}-2 surfaces	-4722.5566	58.6	74.1
PPN-N83@Pd_{23}-top	-4722.5486	79.5	52.7

Table T4: NPA charges of Pd atoms in Pd_{23} cluster interacting with PPN monomer

Atom	**Pd_{23}**	**PPN-ring B @ Pd_{23}-surface**	**PPN-ring C @ Pd_{23}-surface**	**PPN-2rings @ Pd_{23}-2sufaces**	**PPN-N83 @ Pd_{23}-top**
Pd1	-1.26955	-1.29035	-1.28795	-1.06199	-1.26111
Pd2	0.21005	0.19749	0.19882	0.15684	0.19190
Pd3	-0.42800	-0.30240	-0.31637	-0.41202	-0.49877
Pd4	0.21356	0.13180	0.12528	0.19401	0.20685
Pd5	**0.01763**	-0.13818	-0.07773	0.01032	-0.02929
Pd6	0.20475	0.18129	0.17914	0.18016	0.19558
Pd7	0.02444	0.05373	0.06324	-0.01456	0.01583
Pd8	**0.05995**	0.07108	0.08719	0.16114	-0.05344
Pd9	0.06005	0.04115	0.02561	0.05680	0.08895
Pd10	0.02434	0.05983	0.06239	0.09027	0.03702
Pd11	0.11618	0.00089	-0.00782	0.16356	0.11894
Pd12	-0.28965	-0.26423	-0.25994	-0.46755	-0.33217
Pd13	**0.07413**	0.03684	0.02723	-0.18728	0.04562
Pd14	**0.07410**	0.02429	0.01771	0.05652	0.08863
Pd15	-0.28973	-0.21924	-0.20688	-0.14957	-0.30123
Pd16	0.21833	0.16879	0.16251	0.18039	0.19488
Pd17	**0.19838**	0.24857	0.20365	0.18519	0.18578
Pd18	0.19833	0.18536	0.16982	0.21912	0.16621
Pd19	0.21824	0.18991	0.18988	0.18753	0.19749
Pd20	**0.05744**	0.05755	0.05996	0.03509	0.05121
Pd21	0.12475	0.12178	0.12560	0.08579	0.12489
Pd22	0.12483	0.12487	0.12795	0.14235	0.10524
Pd23	0.05745	0.06676	0.02825	0.04656	0.10523

Table T5: NPA charges of all C/N/H atoms of PPN during the interaction with Pd$_{23}$ cluster

Atom	**PPN**	**PPN-ring B @ Pd$_{23}$-surface**	**PPN-ring C @ Pd$_{23}$-surface**	**PPN-2rings @ Pd$_{23}$-2sufaces**	**PPN-N83 @ Pd$_{23}$-top**
N24	-0.52310	-0.49955	-0.49960	-0.56196	-0.52310
C25	0.17194	0.15908	0.16844	0.19399	0.17166
C26	0.18193	0.16809	0.25417	0.18723	0.18242
C27	0.17283	0.22106	0.16683	0.20026	0.17243
C28	-0.23647	-0.22960	-0.21461	-0.27113	-0.23671
C29	-0.24089	-0.22647	-0.31759	-0.2036	-0.24188
C30	-0.23880	-0.30804	-0.21548	-0.28152	-0.23840
C31	-0.23664	-0.21513	-0.23876	-0.20226	-0.23656
C32	-0.24049	-0.21427	-0.30401	-0.23758	-0.24019
C33	-0.23837	-0.28611	-0.22982	-0.27396	-0.23852
C34	-0.20388	-0.20213	-0.19418	-0.25051	-0.20411
C35	-0.00057	0.00313	-0.00153	0.00133	-0.00206
C36	-0.20406	-0.21304	-0.19566	-0.23219	-0.20377
C37	-0.20464	-0.19768	-0.17860	-0.23584	-0.20437
C38	-0.19563	-0.18166	-0.20606	-0.18668	-0.19484
C39	-0.20406	-0.21214	-0.20083	-0.24281	-0.20409
C40	-0.23224	-0.21430	-0.20703	-0.24163	-0.23216
C41	-0.23781	-0.21990	-0.28428	-0.21288	-0.23747
C42	-0.23342	-0.26943	-0.21358	-0.30354	-0.23292
H43	0.23049	0.23082	0.23450	0.25273	0.23031
H44	0.23389	0.23390	0.26156	0.23369	0.23312
H45	0.23007	0.25950	0.23214	0.25406	0.23025
H46	0.22937	0.23468	0.23579	0.25125	0.22968
H47	0.23049	0.24061	0.26446	0.23311	0.23087
H48	0.22998	0.26665	0.23037	0.26472	0.22959
H49	0.21974	0.22471	0.22612	0.25424	0.21962
H50	0.21964	0.25434	0.22563	0.25854	0.21994
H51	0.21930	0.22524	0.23169	0.25653	0.21973
H52	0.22005	0.22696	0.26349	0.22509	0.22071
H53	0.21944	0.26504	0.22448	0.25957	0.21949
H54	0.21820	0.22384	0.22618	0.25484	0.21836
H55	0.21519	0.21939	0.26385	0.21995	0.21602
H56	0.21817	0.26708	0.22392	0.25880	0.21844
C57	-0.44762	-0.44851	-0.42831	-0.44940	-0.44827
H58	0.23030	0.23234	0.24195	0.23273	0.23252
H59	0.23075	0.23300	0.23776	0.23392	0.23164
C60	-0.01924	-0.02353	-0.01549	-0.02494	-0.01449
C61	-0.21107	-0.21186	-0.20986	-0.21162	-0.20756
C62	-0.20890	-0.20955	-0.20914	-0.21004	-0.20659

C63	-0.20843	-0.20816	-0.20531	-0.20801	-0.20841
H64	0.21481	0.21548	0.21684	0.21529	0.21694
C65	-0.21205	-0.21145	-0.20968	-0.21085	-0.21147
H66	0.22060	0.21985	0.21514	0.22030	0.22259
C67	-0.01936	-0.01659	-0.01444	-0.01589	-0.02519
H68	0.22124	0.22272	0.22392	0.22300	0.21972
H69	0.21422	0.21559	0.21619	0.21582	0.21477
C70	-0.44928	-0.44930	-0.44915	-0.44932	-0.45047
H71	0.22952	0.22995	0.22987	0.22991	0.23370
H72	0.23065	0.23047	0.23058	0.23072	0.23215
C73	-0.02576	-0.02892	-0.03050	-0.02934	-0.00063
C74	-0.20492	-0.20477	-0.20496	-0.20497	-0.18710
C75	-0.21006	-0.21023	-0.21017	-0.21009	-0.20061
C76	-0.22388	-0.22414	-0.22433	-0.22431	-0.19318
H77	0.22411	0.22353	0.22338	0.22329	0.23336
C78	-0.22698	-0.22753	-0.22811	-0.22756	-0.21932
H79	0.21674	0.21640	0.21614	0.21654	0.22150
C80	0.16510	0.16735	0.16883	0.16772	0.16645
H81	0.23078	0.23131	0.23171	0.23127	0.23085
H82	0.23044	0.23086	0.23096	0.23103	0.23402
N83	-0.52326	-0.52322	-0.52316	-0.52323	-0.56089
C84	0.17241	0.17121	0.17056	0.17107	0.19592
C85	-0.23881	-0.23862	-0.23848	-0.23854	-0.23523
C86	-0.23900	-0.23818	-0.23737	-0.23796	-0.28197
C87	-0.20383	-0.20364	-0.20376	-0.20371	-0.17608
H88	0.22978	0.22969	0.22955	0.22969	0.23680
C89	-0.20392	-0.20360	-0.20336	-0.20361	-0.20748
H90	0.23011	0.23024	0.23044	0.23029	0.26555
C91	-0.23338	-0.23219	-0.23156	-0.23209	-0.19680
H92	0.21954	0.21998	0.22001	0.21997	0.22703
H93	0.21964	0.22012	0.22042	0.22017	0.25095
H94	0.21820	0.21878	0.21899	0.21880	0.22946
C95	0.17213	0.17147	0.17091	0.17127	0.17144
C96	-0.23794	-0.23816	-0.23797	-0.23817	-0.20195
C97	-0.23878	-0.23791	-0.23730	-0.23779	-0.23383
C98	-0.20420	-0.20442	-0.20439	-0.20434	-0.18483
H99	0.22958	0.22907	0.22912	0.22900	0.23400
C100	-0.20407	-0.20358	-0.20351	-0.20349	-0.19314
H101	0.23025	0.23060	0.23062	0.23059	0.23610
C102	-0.23319	-0.23243	-0.23192	-0.23218	-0.20748
H103	0.21946	0.21940	0.21959	0.21951	0.22826
H104	0.21971	0.22023	0.22036	0.22030	0.22618
H105	0.21825	0.21864	0.21883	0.21877	0.22526

Table T6: Natural Bond Orbital (NBO) analysis of Pd_{23} cluster interacting with PPN

Interaction configurations	**Donor NBO (i)**	**Acceptor NBO (j)**	**E(2), kcal/mol**
PPN-ring B@Pd_{23}-surface	LP*(1) C39	LP (5) Pd5	327.3
	LP (5) Pd14	LP (1) C42	121.0
	LP (4) Pd5	LP*(1) C39	14.2
	LP (5) Pd17	σ*(2) C30 – C36	17.2
PPN-ring C@Pd_{23}-surface	LP (5) Pd5	σ*(2) C35–C41	30.4
	LP (5) Pd14	σ*(2) C32–C38	27.7
	σ (2) C35–C41	LP (5) Pd5	12.4
PPN-2rings@Pd_{23}-2 surfaces	LP (4) Pd5	BD*(2) C30–C36	22.7
	LP (5) Pd13	LP*(1) C27	230.6
	LP (4) Pd14	BD*(2) C33–C39	25.3
	LP (5) Pd17	LP (1) C42	109.0
	LP (4) Pd18	σ*(2) C28–C34	13.6
	LP (5) Pd18	σ*(2) C28–C34	12.1
	LP*(6) Pd18	σ*(1) C30–C36	5.7
	LP*(6) Pd18	σ*(1) C33–C3	4.7
	LP (4) Pd20	σ*(2) C37–C40	11.4
	σ (2) C30–C36	LP*(8) Pd13	11.5
	σ (2) C28–C34	LP*(8) Pd18	8.0
PPN-N83 @ Pd_{23}-top	LP (4) Pd8	BD*(2) C86–C89	12.1
	LP (1) N83	LP*(7) Pd17	4.0

Note:

π*, σ* denotes π-antibonding orbital and σ-antibonding one, respectively. LP symbolizes a lone pair of electrons and LP(n) for the n^{th} lone pair of electrons. RY* indicates 1-center Rydberg.

3. Electronics properties of different carboxylic acids used as surrogate models for stearic acid in the HDO reaction on Pd catalyst.

3.1. Butanoic acid (C_3H_7COOH)

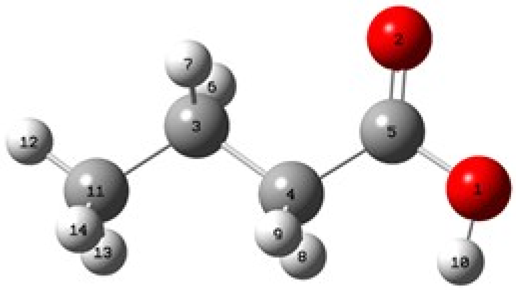

NPA CHARGES

Atom	No	Charge	Core	Valence	Rydberg	Total
O	1	-0.70595	1.99975	6.67801	0.02819	8.70595
O	2	-0.59635	1.99973	6.56383	0.0328	8.59635
C	3	-0.39945	1.99935	4.38131	0.0188	6.39945
C	4	-0.51387	1.99921	4.49878	0.01587	6.51387
C	5	0.84988	1.99945	3.10963	0.04104	5.15012
H	6	0.21204	0	0.78519	0.00277	0.78796
H	7	0.21204	0	0.78519	0.00277	0.78796
H	8	0.22104	0	0.77619	0.00278	0.77896
H	9	0.22104	0	0.77619	0.00278	0.77896
H	10	0.48003	0	0.51677	0.00319	0.51997
C	11	-0.58612	1.99938	4.57625	0.01048	6.58612
H	12	0.2113	0	0.78719	0.00151	0.7887
H	13	0.19719	0	0.80105	0.00176	0.80281
H	14	0.19719	0	0.80105	0.00176	0.80281
	Total	0	11.99686	35.83662	0.16651	48

3.2. Pentanoic acid (C_4H_9COOH)

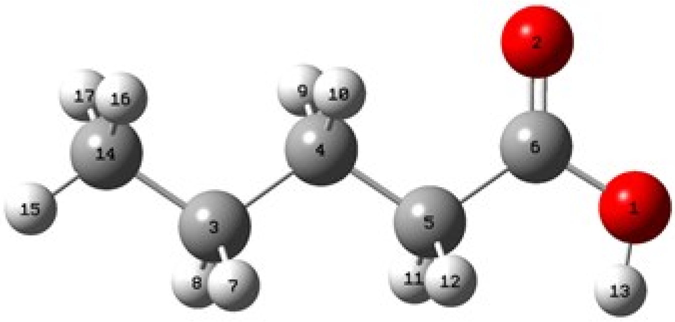

NPA CHARGES

Atom	No	Charge	Core	Valence	Rydberg	Total
O	1	-0.70601	1.99975	6.67814	0.02813	8.70601
O	2	-0.59633	1.99973	6.56384	0.03276	8.59633
C	3	-0.3933	1.99934	4.37862	0.01535	6.3933
C	4	-0.39706	1.99932	4.37727	0.02047	6.39706
C	5	-0.51109	1.99921	4.49609	0.0158	6.51109
C	6	0.85045	1.99945	3.10915	0.04095	5.14955
H	7	0.19141	0	0.806	0.00259	0.80859
H	8	0.19141	0	0.806	0.00259	0.80859
H	9	0.21216	0	0.78509	0.00275	0.78784
H	10	0.21216	0	0.78509	0.00275	0.78784
H	11	0.2217	0	0.77538	0.00293	0.7783
H	12	0.2217	0	0.77538	0.00293	0.7783
H	13	0.48001	0	0.51679	0.0032	0.51999
C	14	-0.58342	1.99938	4.57339	0.01065	6.58342
H	15	0.20509	0	0.79328	0.00164	0.79491
H	16	0.20057	0	0.79755	0.00188	0.79943
H	17	0.20057	0	0.79755	0.00188	0.79943
=======	=======	=======	=======	=======	=======	=======
	Total	0	13.99617	41.81458	0.18925	56

3.3. Hexanoic acid ($C_5H_{11}COOH$)

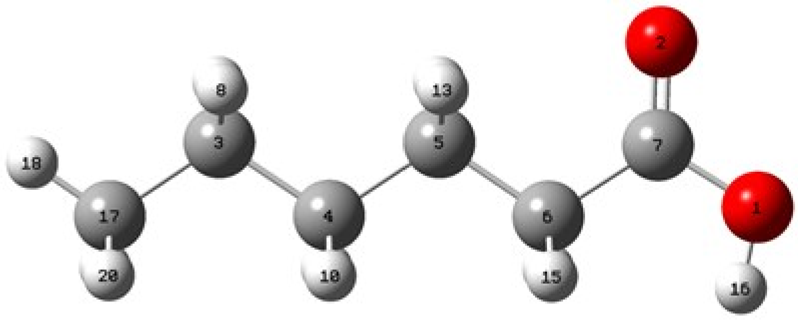

NPA CHARGES

Atom	No	Charge	Core	Valence	Rydberg	Total
O	1	-0.70606	1.99975	6.67817	0.02814	8.70606
O	2	-0.59637	1.99973	6.56391	0.03273	8.59637
C	3	-0.3922	1.99934	4.3773	0.01557	6.3922
C	4	-0.38981	1.99931	4.37418	0.01632	6.38981
C	5	-0.3949	1.99932	4.37532	0.02027	6.3949
C	6	-0.51033	1.99921	4.4955	0.01562	6.51033
C	7	0.85061	1.99945	3.10898	0.04096	5.14939
H	8	0.19503	0	0.80225	0.00272	0.80497
H	9	0.19503	0	0.80225	0.00272	0.80497
H	10	0.19152	0	0.80599	0.00249	0.80848
H	11	0.19152	0	0.80599	0.00249	0.80848
H	12	0.21285	0	0.78431	0.00284	0.78715
H	13	0.21285	0	0.78431	0.00284	0.78715
H	14	0.22168	0	0.77545	0.00287	0.77832
H	15	0.22168	0	0.77545	0.00287	0.77832
H	16	0.48004	0	0.51677	0.00319	0.51996
C	17	-0.58393	1.99938	4.5741	0.01045	6.58393
H	18	0.20609	0	0.7923	0.00161	0.79391
H	19	0.19734	0	0.80082	0.00184	0.80266
H	20	0.19734	0	0.80082	0.00184	0.80266
	Total	0	15.99549	47.79415	0.21036	64

3.4. Stearic acid ($C_{17}H_{35}COOH$)

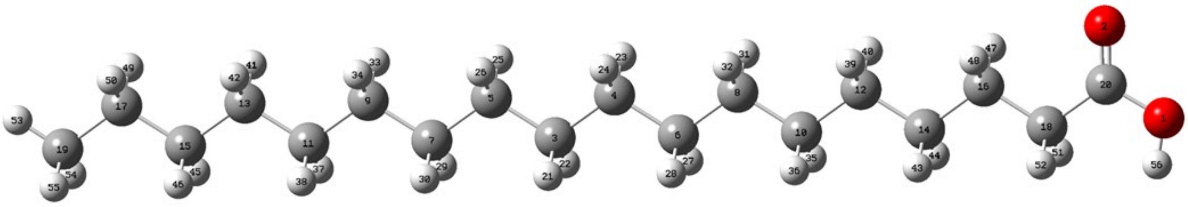

NPA CHARGES

Atom	No	Charge	Core	Valence	Rydberg	Total
O	1	-0.7061	1.99975	6.67823	0.02812	8.7061
O	2	-0.59641	1.99973	6.56395	0.03273	8.59641
C	3	-0.29798	1.99932	4.27057	0.02809	6.29798
C	4	-0.41034	1.99937	4.38522	0.02575	6.41034
C	5	-0.41024	1.99937	4.38512	0.02575	6.41024
C	6	-0.38896	1.99931	4.36994	0.0197	6.38896
C	7	-0.38898	1.99931	4.36995	0.01971	6.38898
C	8	-0.38591	1.99931	4.37014	0.01646	6.38591
C	9	-0.38559	1.99931	4.36988	0.0164	6.38559
C	10	-0.38527	1.99931	4.36972	0.01624	6.38527
C	11	-0.38532	1.99931	4.36972	0.01629	6.38532
C	12	-0.38573	1.99931	4.36999	0.01643	6.38573
C	13	-0.38612	1.99931	4.37049	0.01631	6.38612
C	14	-0.3866	1.99931	4.37127	0.01602	6.3866
C	15	-0.38809	1.99931	4.3723	0.01647	6.38809
C	16	-0.39382	1.99932	4.37437	0.02014	6.39382
C	17	-0.39161	1.99934	4.37693	0.01535	6.39161
C	18	-0.51007	1.99921	4.49528	0.01558	6.51007
C	19	-0.58344	1.99938	4.57369	0.01037	6.58344
C	20	0.85053	1.99945	3.10907	0.04095	5.14947
H	21	0.18138	0	0.81052	0.0081	0.81862
H	22	0.18138	0	0.81052	0.0081	0.81862
H	23	0.19284	0	0.8044	0.00276	0.80716
H	24	0.19284	0	0.8044	0.00276	0.80716
H	25	0.19261	0	0.80462	0.00277	0.80739
H	26	0.19261	0	0.80462	0.00277	0.80739
H	27	0.19239	0	0.8048	0.00281	0.80761
H	28	0.19239	0	0.8048	0.00281	0.80761
H	29	0.19236	0	0.80482	0.00282	0.80764
H	30	0.19236	0	0.80482	0.00282	0.80764

H	31	0.19355	0	0.80373	0.00273	0.80645
H	32	0.19355	0	0.80373	0.00273	0.80645
H	33	0.19261	0	0.80465	0.00274	0.80739
H	34	0.19261	0	0.80465	0.00274	0.80739
H	35	0.19254	0	0.80476	0.0027	0.80746
H	36	0.19254	0	0.80476	0.0027	0.80746
H	37	0.1925	0	0.80478	0.00272	0.8075
H	38	0.1925	0	0.80478	0.00272	0.8075
H	39	0.19573	0	0.80154	0.00273	0.80427
H	40	0.19573	0	0.80154	0.00273	0.80427
H	41	0.1926	0	0.80464	0.00276	0.8074
H	42	0.1926	0	0.80464	0.00276	0.8074
H	43	0.19213	0	0.80529	0.00258	0.80787
H	44	0.19213	0	0.80529	0.00258	0.80787
H	45	0.19178	0	0.80558	0.00264	0.80822
H	46	0.19178	0	0.80558	0.00264	0.80822
H	47	0.21275	0	0.78445	0.0028	0.78725
H	48	0.21275	0	0.78445	0.0028	0.78725
H	49	0.19169	0	0.80558	0.00272	0.80831
H	50	0.19169	0	0.80558	0.00272	0.80831
H	51	0.22162	0	0.77551	0.00287	0.77838
H	52	0.22162	0	0.77551	0.00287	0.77838
H	53	0.2033	0	0.79506	0.00164	0.7967
H	54	0.19702	0	0.8011	0.00188	0.80298
H	55	0.19702	0	0.8011	0.00188	0.80298
H	56	0.48004	0	0.51676	0.0032	0.51996

==

	Total	0.00349	39.98737	119.4892	0.51994	159.9965

4. Details and results from VASP calculations

4.1. Justify on choosing level of theory: optB88-vdW functional

All the DFT calculations including the interaction between PPN framework with the Pd nanoparticle and the conversion of butanoic acid on different Pd structures (terrace sites and stepped sites) were performed using the optimized Becke88 functional (optB88) coupled with the non-local vdW-DF correlation (optB88-vdW) developed by Klimeš *et al.*[14-16] This is one of the best appropriate level of theory for those calculations since the dispersion plays very important role in the interaction of aromatics and carboxylic acid with metal surfaces/NPs, which was also reported in earlier studies.[16-22] We also performed a benchmarking evaluations (in comparison with experimental data) for the performance of the chosen optB88-vdW functional in describing the adsorption of benzene (which is the representative molecule for the PPN structure in our study) and the adsorption of formic acid (which represents for the butanoic acid in our study) on several flat terrace sites of Pd(111), Ni(111), Cu(111) and Pt(111) surfaces. The computed adsorption energies using optB88-vdW functional match quite well with experimental data in literature, and the results are shown in Table T7 below. It is worth noting that the computed results performed using the optB88-vdW functional in this study are very close to the reported values in earlier theoretical studies.[16-18]

Table T7. Computed adsorption energy of benzene and formic acid using the optB88-vdW functional on different transition metals at the coverage of 1/16 ML.

Adsorption energy of benzene		
Surface	*Calculated energy in this study*	*Experimental energy and reference*
Pd(111)	-191	-197[17]
Pt(111)	-192	-183[22]
Ni(111)	-174	-188[22]
Cu(111)	-72	-68[18]
Adsorption energy of formic acid		
Surface	*Calculated energy in this study*	*Experimental energy and reference*
Ni(111)	-81	-75.2[23]
Pt(111)	-71	-65.0[24]
Cu(111)	-51	-54[25]

We also computed the adsorption of a monomer TPA (triphenylamine) and one unit of the Porous Organic Polymeric network (called PPN) on terrace sites of the reduce model Pd_{332} cluster using both the conventional PBE functional and the optB88-vdW functional to evaluate the contribution of dispersion into the interaction between those poly-aromatic rings compounds and the surfaces. The optimized structures of TPA and PPN adsorbed on Pd$_{332}$ cluster are shown in Figure S11. The adsorption energy of TPA computed using PBE and optB88-vdW functionals are -53 and -231 kJ/mol, while the adsorption energy of PPN computed using PBE and optB88-vdW functionals are -67 and -239 kJ/mol, respectively. The obtained data showed that there was a huge difference in the computed adsorption energies for those aromatic compounds if the dispersion correction was not incorporated, and demonstrate the necessity of choosing the proper functional for the DFT calculations in this study.

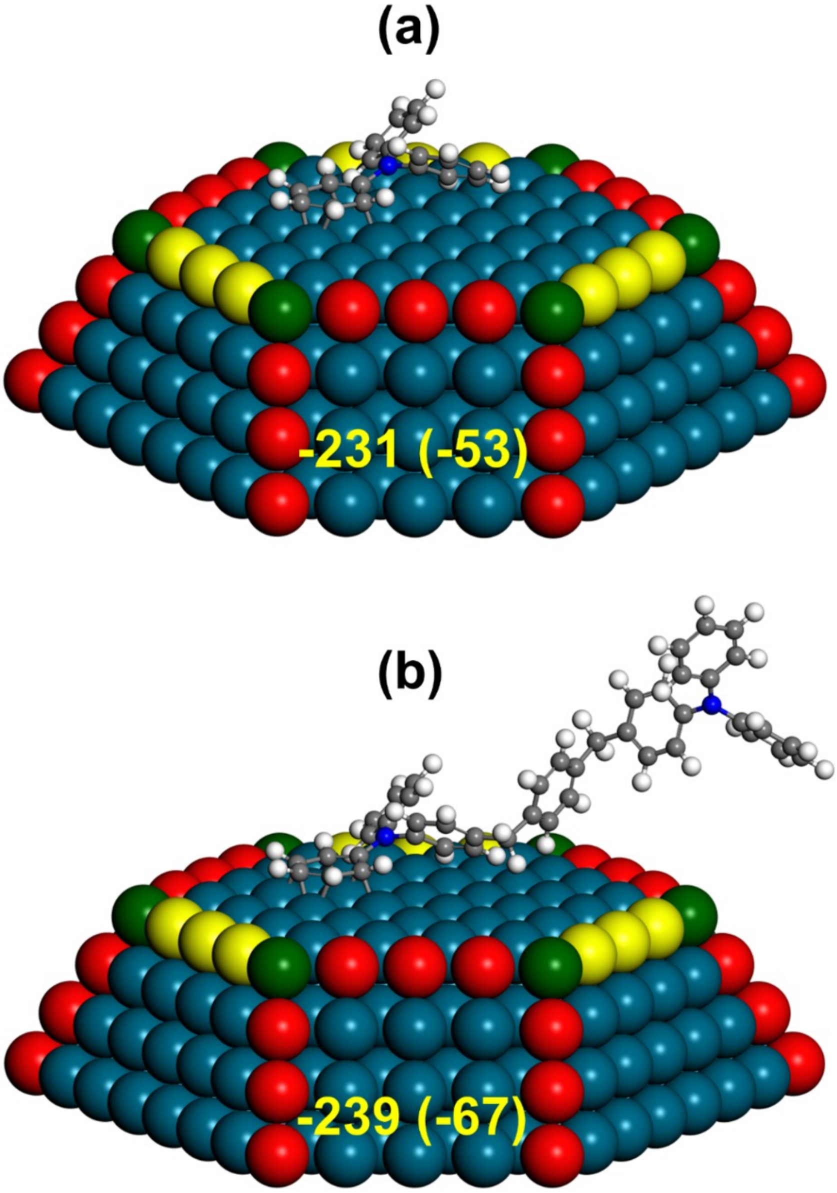

Figure S11. (a) Computed adsorption energies of TPA and (b) PPN on terrace sites of the reduce model of Pd$_{332}$ cluster using both the optB88-vdW functional and the PBE functional. The values obtained by PBE functional are shown in parentheses.

In the case of butanoic acid conversion on Pd surfaces, the inclusion of vdW functional also has slight influence to the adsorption energy of the butanoic acid. The computed adsorption energies for butanoic acid on terraces and B5 step Pd sites using PBE functional are -63 and -81 kJ/mol, respectively. When the optB88-vdW functional was used, the computed adsorption energies for butanoic acid on terraces and B5 step Pd sites are -83 and -95 kJ/mol, respectively. However, the influence of vdW interaction to subsequent steps after initial adsorption is much smaller. It is in excellent consistent with our earlier test in Trinh *et al.*[19] The comparison for the performance between optB88-vdW and the PBE functionals during the conversion of butanoic acid on Pd(111) surface are presented in Table T8 below:

Table T8. Computed adsorption energies ΔE_{ads} and activation barriers E_a (kJ/mol) for butanoic adsorption and activation on Pd(111) surface using different functionals.

Functional	**PBE**	**optB88-vdW**
Initial Adsorption:	ΔE_{ads} (kJ/mol)	
$C_3H_7COOH(g) + * \rightarrow C_3H_7COOH*$	-63	-83
Reactions at step 1:	E_a (kJ/mol)	
$C_3H_7COOH* + * \rightarrow C_3H_7COO* + H*$	61	63
$C_3H_7COOH* + * \rightarrow C_2H_5\text{-}CH\text{-}COOH* + H*$	125	117
$C_3H_7COOH* + * \rightarrow CH_3\text{-}CH\text{-}CH_2COOH* + H*$	135	129
$C_3H_7COOH* + * \rightarrow CH_2\text{-}CH_2CH_2COOH* + H*$	136	133
$C_3H_7COOH* + * \rightarrow C_3H_7CO* + OH*$	143	146
Reaction at step 2	E_a (kJ/mol)	
$C_3H_7COO* + * \rightarrow C_2H_5\text{-}CH\text{-}COO* + H*$	132	131
$C_3H_7COO* + * \rightarrow CH_3\text{-}CH\text{-}CH_2\text{-}COO* + H*$	142	145
$C_3H_7COO* + * \rightarrow CH_2\text{-}CH_2\text{-}CH_2\text{-}COO* + H*$	146	149
$C_2H_5\text{-}CH\text{-}COOH* + * \rightarrow CH_3\text{-}CH\text{-}CH\text{-}COOH* + H*$	78	81

4.2. Justify on choosing the models for calculations.

In our calculations, we started initially with the full size cluster of 1289 atoms Pd (called Pd_{1289} cluster) in a cuboctahedra shape as the model for the 3 nm Pd NP (the size of 3nm was detected from experiment such as TEM, XRD… as presented in Fig. 3 and Fig. 5 of the main text). This cluster was also used for 3 nm size Ru particle to explain the high activity of B5 step sites during the ammonia synthesis in the study of Honkala et al.[26] Due to the symmetric structure of this cluster and to make the calculations more efficient, we then trimmed down to keep the upper half of this cluster involving the only the top 4 layers (called reduced Pd_{332} cluster) to study the interaction between the Pd NP and the Porous Organic Polymer frame structure, which is illustrated in the Figure S12 below. The similar reduce-cluster model has also been used in a recent study by Zhou et al.[27] to investigate methane dry reforming on Cu-Ru nano-particles. The investigation on the interaction between Pd NPs and the frame structure of the polymer on this reduce cluster (presented later) showed that there is a high density of B5 and F4 step sites on the Pd NPs grew anchoring on the Porous Organic Polymer substrate.

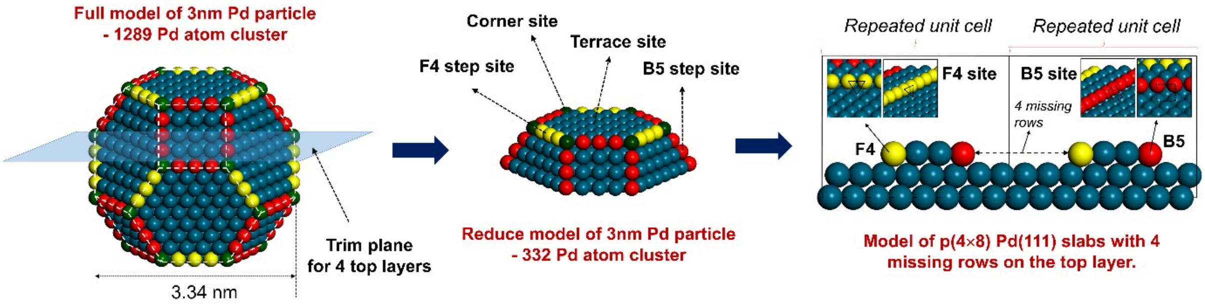

Figure S12. The creation of reduce model including 332 Pd atoms cluster from the full 1289 Pd atoms cuboctahedra cluster of 3 nm Pd nanoparticle by trimming the 4 top layers of the full model. F4 sites, B5 sites and corner sites are highlighted by yellow, green and red balls, respectively. The use of p(4x8) Pd(111) slab with 4 missing rows on the top layer to represent Pd_{322} cluster in the carboxylic HDO activity investigation is also shown.

Besides, we have also computed the binding energy of TPA (triphenylamine) on a two different reduced model with 4 top-layers and 5 top-layers, and found the binding energies are very close to each other, which confirms that the reduced model including 4 top-layers is enough for the calculations (Figure S13 below).

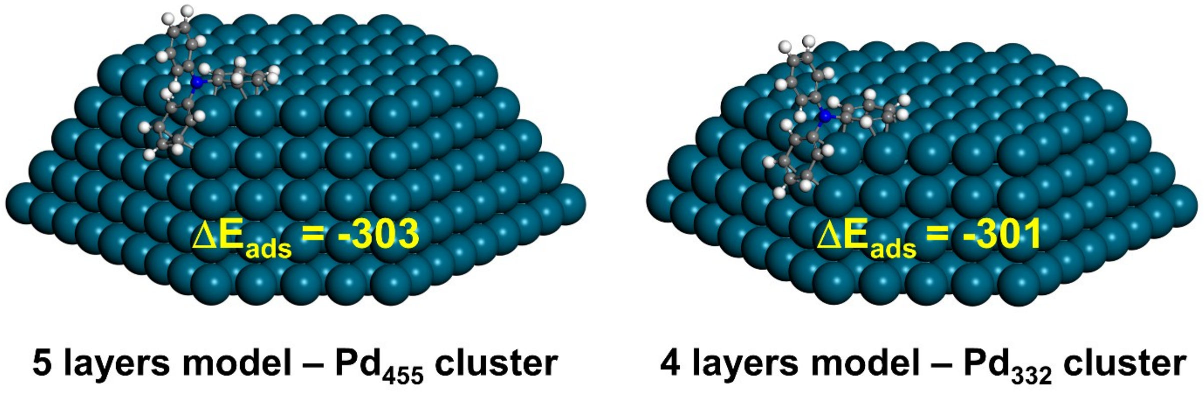

Figure S13. Computed adsorption energy of TPA (triphenylamine) on two different reduce models including the top 5 layers and top 4 layers of the full model in Fig. S12.

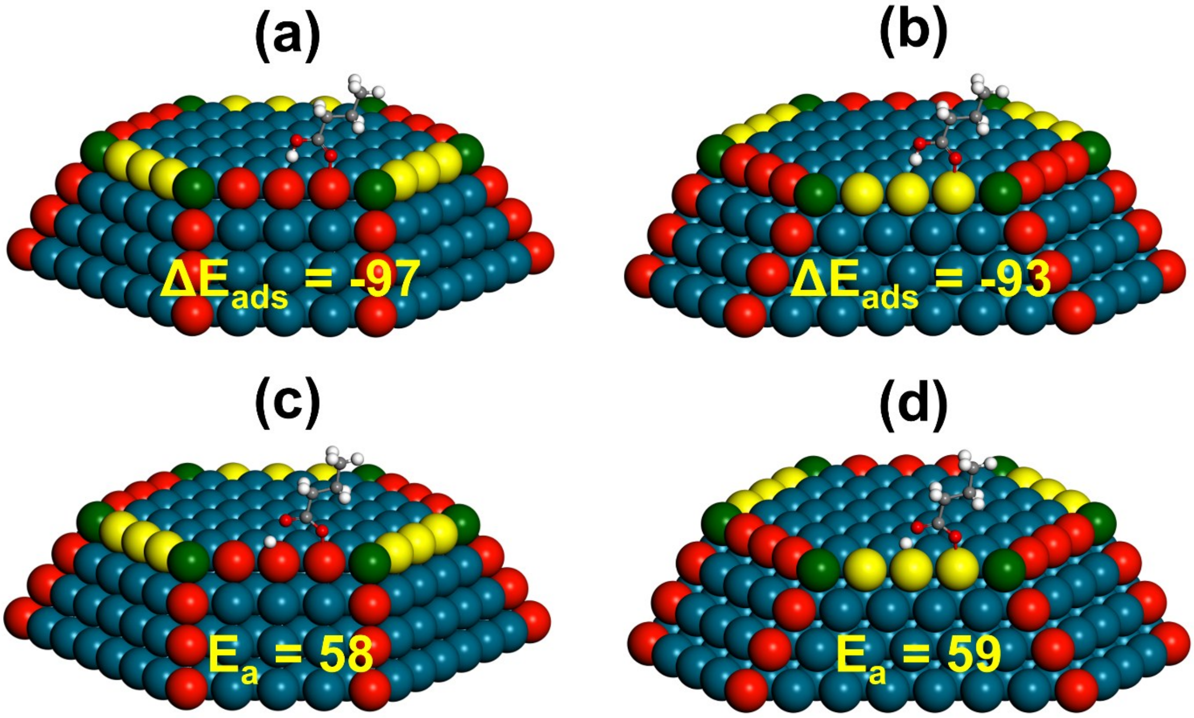

Figure S14. Adsorption configuration and adsorption energies (in kJ/mol) of butanoic acid at B5 step site (a) and F4 step site (b) on Pd_{332} cluster; Transition state of initial OH activation and the computed activation barriers (in kJ/mol) of butanoic acid at B5 step site (c) and F4 step site (d) on Pd_{332} cluster.

For locating the transition states during the reaction by the Climbing-Nudged Elastic Band (Cl-NEB) method, using the reduce cluster is somehow still a quite large scale. Typically, in the Cl-NEB method, a series of intermediate states (six to ten intermediate states) distributed along the initial reaction path connecting a reactant and a product state are simultaneously optimized while restricting atomic motions to hyperplanes perpendicular to the reaction path, making it not computationally efficient for large systems. Therefore, to make the computational evaluation more efficient, we then build the p(4x8) Pd(111) slab with 4 missing rows on the top layer to create both F4 step sites and B5 step sites in one model (highlighted in Fig. 1d of the main text), allowing us to evaluate their activities in the HDO conversion of carboxylic acid. We also calculated and compared the adsorption and activation of butanoic acid on the B5 and F4 step sites of the reduce Pd_{332} cluster and on the B5 and F4 step sites of the p(4x8) with 4 missing row model (using optB88-vdW functional) as showed in Table T9, and the structures of butanoic acid adsorption and activation at B5 and F4 step sites on Pd_{332} cluster are presented in Figure S14.

Table T9. Computed adsorption energies ΔE_{ads} and activation barriers E_a (kJ/mol) for butanoic adsorption and activation at B5 and F4 step sites on Pd_{332} cluster and on p(4x8) Pd(111) slab with 4 missing row model, calculated using optB88-vdW functional.

	Pd_{332} cluster	p(4x8) Pd(111) with 4 missing row model
Adsorption energy of butanoic acid at B5 step site	-97	-95
Adsorption energy of butanoic acid at F4 step site	-93	-94
Barrier of OH activation on B5 site	58	56
Barrier of OH activation on F4 site	59	57

In our study, the Porous Organic Polymer Network has been synthesized by the polymerization of two monomer units: triphenylamine (TPA) and p-xylene, generating the porous polymer support and later the Pd nanoparticles was growed inside the pores of this polymer. We also agree with the reviewer that using TPA as a representative molecule to study the structure of Pd NPs anchoring onto the polymer substrate might not be the best relevant, therefore we have replaced all the calculations for TPA adsorption on Pd nanoparticle by the adsorption of one full unit of our polymer structure, called *um*PPN molecule. The structure of the *um*PPN unit molecule is shown in Figure S15 below and it is a very good representative molecule to study the interaction between Pd nano-particles and the Porous Polymer frame-structure since it contains all the two-monomer units of the polymer: TPA and p-xylene.

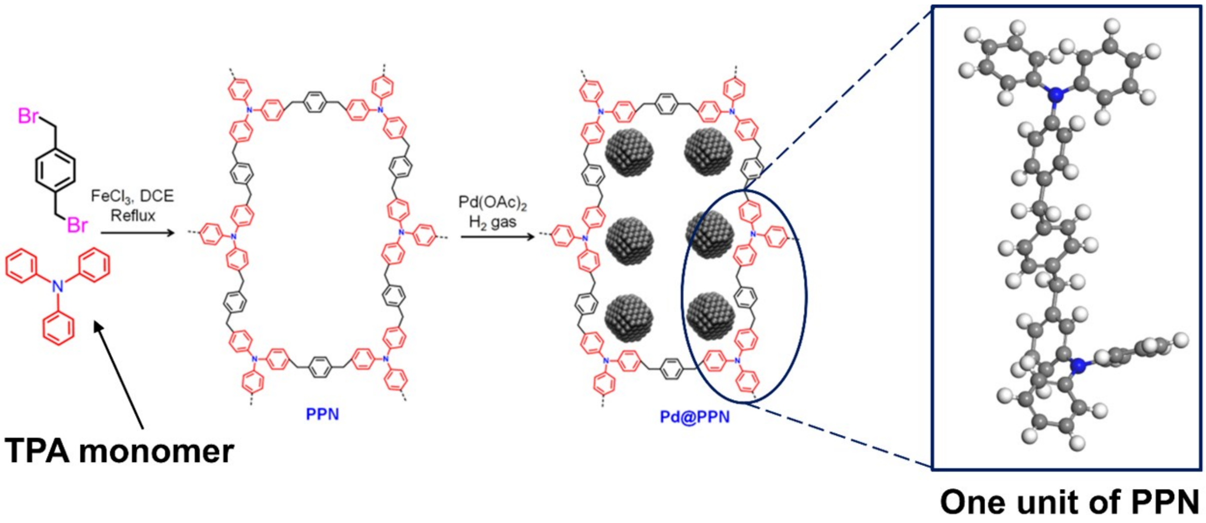

Figure S15. The structure of PPN unit molecule, which was used to represent the Porous Polymer frame-structure in interaction with Pd NPs.

4.3. Higher coverage of TPA adsorption on Pd_{322} cluster

To evaluate whether is there a possibility of blocking all B5 and F4 steps sites on Pd_{322} cluster by the polymer structure, we evaluated the adsorption of TPA molecules on Pd_{322} cluster at higher coverage. Due to the bulky structure of the TPA molecule, the steric effect plays important role in preventing two-monomer unit adsorb adjacently to each other. When two TPA fragments co-adsorb on the step edge of Pd_{332} cluster, due to the repulsion between adjacent benzene rings, two TPA molecules prefer to adsorb far away from each other. It could be seen in Figure S14 below that the configuration where two TPA molecules are next to each other (Fig. S14a) is ~100 kJ/mol less stable than the configuration where two TPA molecules adsorb at two corner sites and far away from each other (Fig. S14b). Therefore, the coverages of the monomer adsorb at step edge might not be high enough to block all step sites (they rather block all corner sites and cover large portion of terrace sites), leaving plenty free step sites to facilitate the HDO reaction.

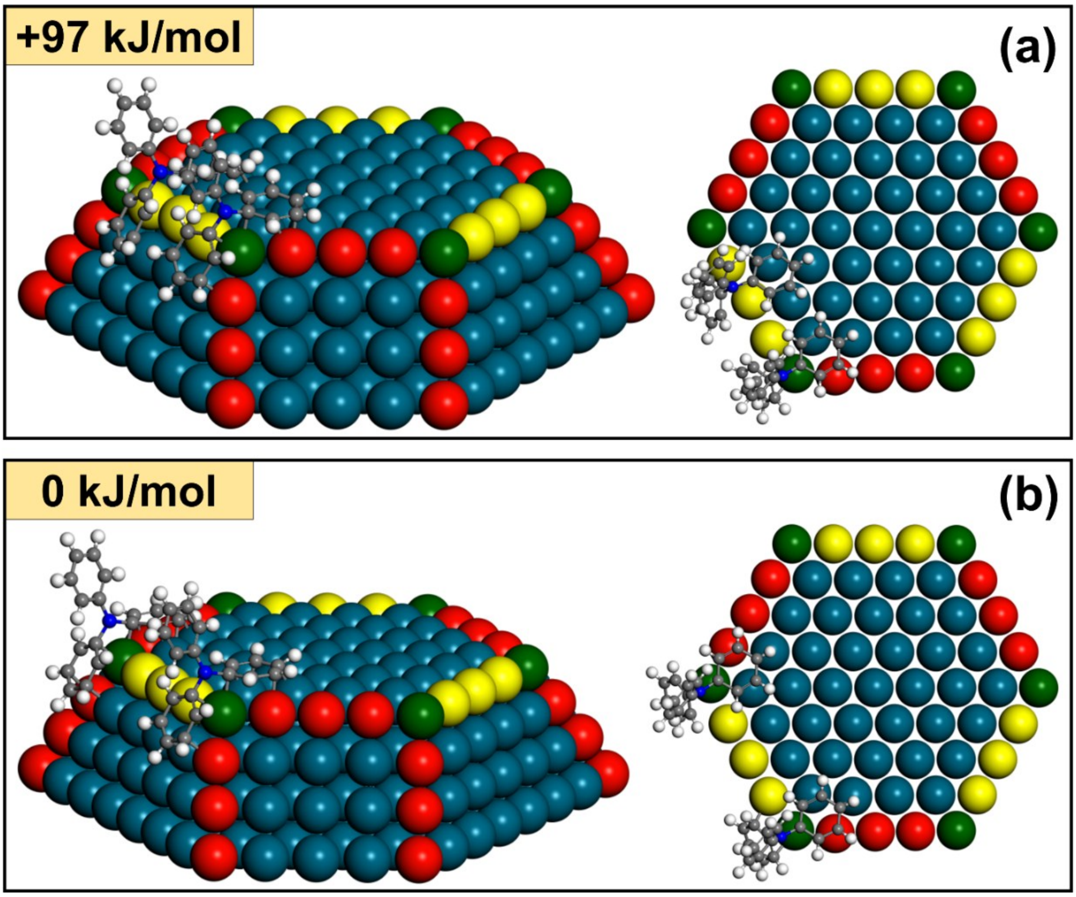

Figure S16. Two different configurations for the co-adsorption of two TPA molecules on Pd_{332} cluster: (a) Two TPA molecules co-adsorb next to each other and (b) Two TPA molecules adsorb at each corner sites and far away. The side view and top view are presented for each configurations. Binding energies relative to the more stable configuration (configuration b) are also shown. Color code is the same as Fig. S12.

4.4. Transition states of butanoic acids HDO conversion on terrace Pd(111) surface.

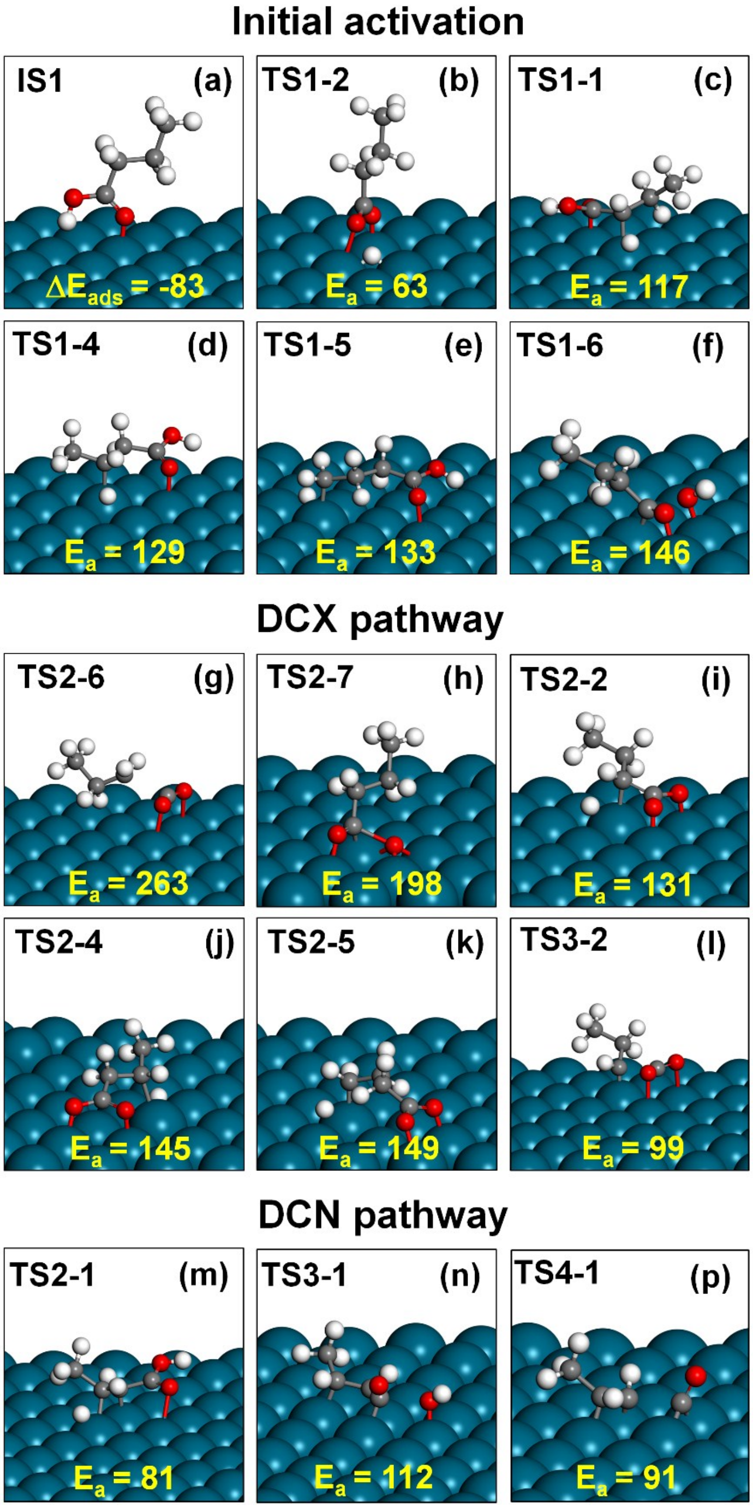

Figure S17. (a) Adsorption of butanoic on Pd(111). (b) Initial O-H activation. (c) Initial C_α-H activation. (d) Initial C_β-H activation. (e) Initial C_γ-H activation. (f) Initial CO-OH scission. The subsequent conversion of butanoic acid via the DCX pathway after the initial O-H activation: (g) Decarboxylation. (h) C-O dissociation. (i) C_α-H activation. (j) C_β-H activation. (k) C_γ-H activation. (l) Decarboxylation in the 3rd step. Subsequent conversions of butanoic acid via the DCN pathway after the initial C_α-H activation: (m) C_β-H activation in 2nd step. (n) CO-OH scission in 3rd step. (p) Decarbonylation in 4th step.

To setup the reference for evaluating the activity of steps sites during the HDO on Pd@PPN catalyst, we revisited the activation and conversion of fatty acid on Pd terrace sites of the p(4×4) Pd(111) periodic slab model via both DCX and DCN pathways using butanoic acid as the model compound. Butanoic acid adsorbs on Pd(111) surface with an adsorption energy of -83 kJ/mol (Figure S17a). Initially, the most feasible activation of butanoic acid on Pd(111) surface could be processed via OH activation with a barrier of 63 kJ/mol (Fig. S17b). C-H bond activations at different positions of butanoic acid are more difficult than OH activation. Among all C-H activations, the C_α-H activation has the lowest barrier of 117 kJ/mol, while the C_β-H and C_γ-H activations have slightly higher barriers of 129 and 133 kJ/mol, respectively (Figs. S17c-e). The similar barriers of C_β-H (middle position) and C_γ-H (secondary terminal position) activations again justified the appropriateness of using butanoic acid as the representative model for long liner-chain stearic acid in this study. The dehydroxylation reaction of the carboxylic acid function group forming surface species $C_3H_7CO^* + OH^*$ has the highest barrier of 146 kJ/mol and therefore is the most difficult reaction to be occurred (Fig. S17f).

The subsequent conversion of butanoic acid processed via the initial O-H activation followed by DCX mechanism is more difficult. Indeed, the decarboxylation reaction forming CO_2 (Fig. S17g) has very high activation barrier of 263 kJ/mol. The deoxygenation reaction involving the dissociation of C=O bond from the adsorbed butyrate (Fig. S17h) has the activation barrier of 198 kJ/mol, in consistent with the barrier of 188 kJ/mol computed for C=O scission from adsorbed formate in Mavrikakis et al.[28] However, the very high barriers for reactions in Figs. S17g,h hinder those reactions to be occurred at our reaction temperature.[29, 30] The most feasible reaction at the 2nd stage after initial OH dissociation is the C_α-H activation (barrier energy of 131 kJ/mol, Fig. S17i), while C-H activations at other positions have higher barriers (Figs. S17j,k). After C_α-H activation in step 2, the decarboxylation reaction in subsequent step (step 3) is much more feasible with the barrier of 99 kJ/mol (Fig. S17l), releasing CO_2 and forming the C3 hydrocarbon product, with one carbon atom less than the initial butanoic acid resource.

Finally, we observe that if the conversion of butatonic acid is processed via the initial C_α-H activation followed by the DCN mechanism, subsequent conversion is easier than the DCX pathway. Indeed, the C_β-H activation at the 2nd step is easier with a barrier of only 81 kJ/mol (Fig. S17m), followed by the subsequent dehydroxylation in step 3 with activation barrier of 112 kJ/mol (Fig. S17n). The DCN reaction is then occurred in the next step 4 with computed activation barrier of 91 kJ/mol (Fig. S17p), releasing CO and forming the C3 hydrocarbon product. All of the data presented herein agrees very well with the data reported earlier and is also consistent with experimental observations in the literature.[31-33]

4.5. RDO path on terrace site

4.5.1. Hydrogenation-dehydration pathway via the Hydrogen-shuttling mechanism.

The mechanism for HDO reaction of linear chain acid on Pd(111) surface has been comprehensively studied in literature.[32-34] It is widely accepted that there are three possible mechanisms for the HDO of carboxylic acids: (i) the decarbonylation (DCN) pathway where oxygen atoms are removed from the initial carboxylic acids reactant in the form of CO, (ii) the decarboxylation (DCX) where oxygen atoms are removed in the form of CO_2 and (iii) the reductive deoxygenation (RDO) where oxygen atoms are removed in the form of water (also called as hydrogenation-hydrodehydration pathway). In the first two cases, the number of carbon atoms in the products is one atom less than in the reactant molecule while for the last case, the number of carbon atoms of the product remained identical as the initial reactant. There is a general agreement from experimental studies in literature that Pd-based catalyst favors the DCX and DCN pathway of carboxylic acids over the RDO pathway in producing the product with one less carbon atom.[35-38] Besides, to facilitate the RDO mechanism, more hydrogen is consumed, however its supply is being in short in refineries and facing growing demand for other competitive applications such as CO_2 reduction, fuel cell… and therefore developing the catalyst that can facilitate the RDO pathway is less desirable.[39-41]

The reductive deoxygenation (RDO) pathway produces the final alkane product with the same carbon atom as in carboxylic acid resource, which was reported to be feasible at higher Hydrogen pressure.[35-37, 42-47] This pathway can be initially processed by the hydrogen-shuttling mechanism, where water acts as a hydrogen shuttle to transfer the adsorbed H on Pd(111) surface to the OH group of butanoic acid and facilitating the dehydration, forming H_2O, as shown in Figure S18. The activation barrier for this reaction is 126 kJ/mol. In the Initial state, water is located in the vicinity of the adsorbed butanoic acid and surface H atom on Pd surface. In the transition state, one H atom of water molecule is transferred to the carboxylic OH group of butanoic acid facilitating the dehydroxylation, while the surface H adsorbed in Pd surface is transferred to the water molecule simultaneously in the concerted mechanism. This type of water mediated H-shuttling mechanism has also been reported in literature for the waterassisted dehydroxylation from HCOH on Ru catalyst,[48] hydrogenation of adsorbed CO on Co(111) surface[49] and formyl C-H dissociation from glucose on CuO catalyst.[50] However, it should be mentioned that this type of H-shuttling reaction will suffer from extra entropic energy penalty for locating the water molecule to the exact positon in the transition state, as was reported by Gunasorria *et al.*[49] and Amaniampong *et al.*[51], making it further less favourable compare to the DCX and DCN pathways and will only be feasible at high enough pressure of hydrogen. This observation could explain the high selectivity towards the DCX and DCN pathways obtained from the HDO of carboxylic acids obtained in our study. It should be noted that direct dehydroxylation of butanoic acid without the presence of water and surface hydrogen has the higher activation barrier of 146 kJ/mol (Fig. S17f) and is therefore less feasible than the Hydrogen-shuttling pathway.

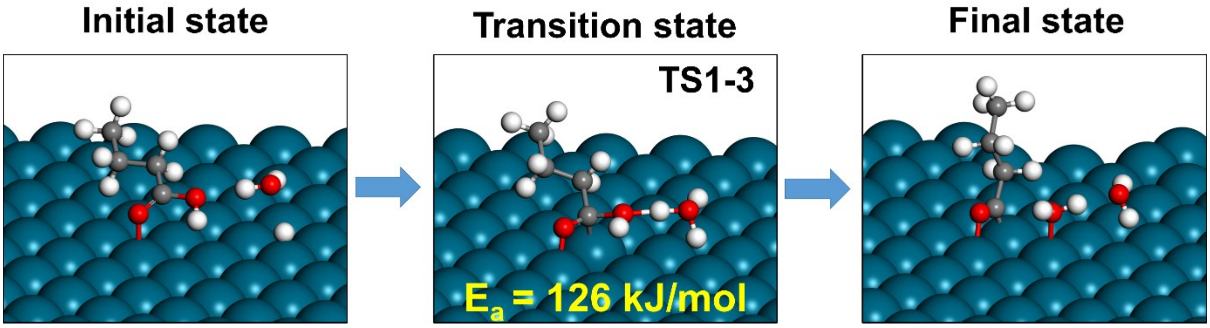

Figure S18. Initial state, Transition state and Final state for the Hydrogenation-dehydration reaction on terrace Pd(111) surface via the Hydrogen-shuttling mechanism

4.5.2. RDO pathway via the two-step Hydrogenation-dehydroxylation mechanism

Instead of initiating by the concerted pathway via the Hydrogen-shuttling mechanism, the Hydrogenation-dehydration pathway can be processed via the two-step mechanism: first step is the hydrogenation to the butanoic acid forming a complex intermediate C_3H_7CHOOH as shown in Figure S19; following by the second step of dehydroxylation from that complex intermediate generating C_4 aldehyde. The transition states and activation barriers for those reactions are shown in Figure S19.

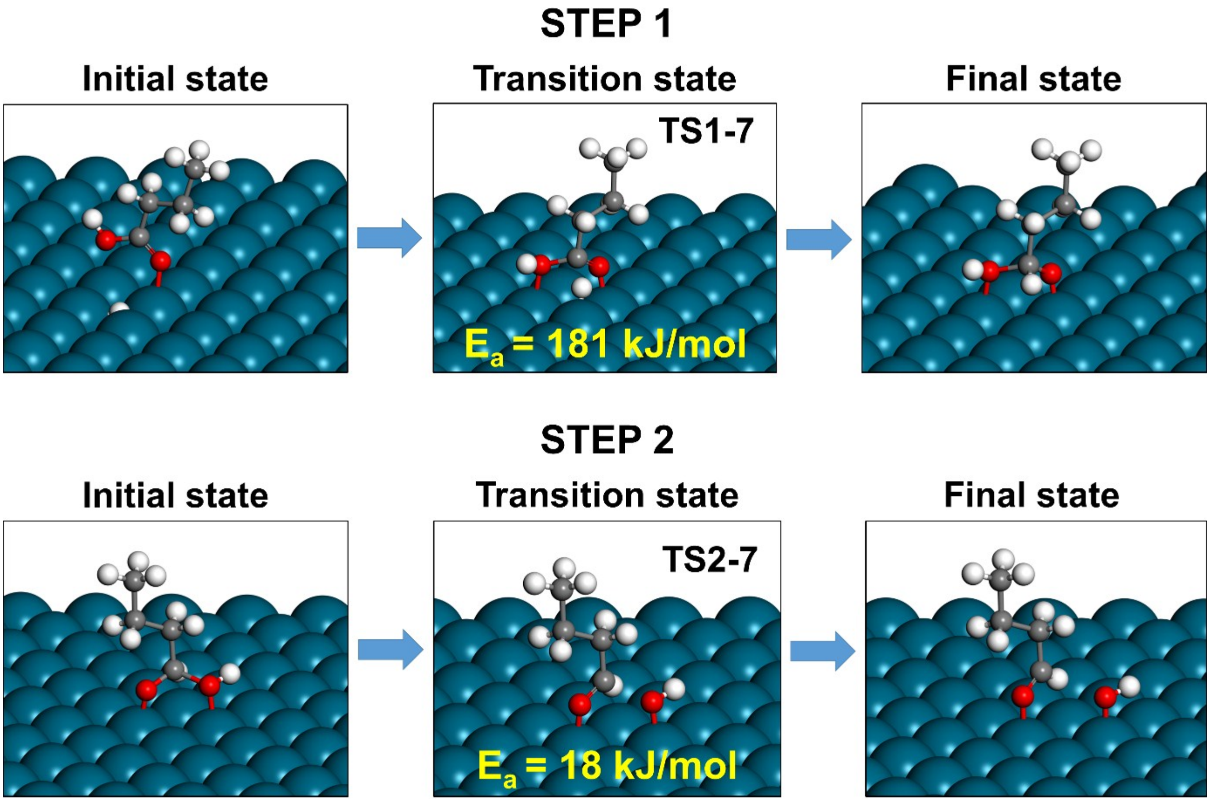

Figure S19. Initial states, Transition states and Final states for the reactions along the two-step Hydrogenation-dehydroxylation mechanism on terrace Pd(111) surface

The formation of the complex intermediate by hydrogenation into the carboxylic acids in step 1 has been proposed and validated by experiments during the oxidation of aldehyde on Pt(111) and Au(111) by Zope et al.[52], hydrogenation of unsaturated ketones and unsaturated aldehydes on transition metals catalyst[53], or selective oxidation of glycerol[54] and glucose[51] on CuO surface. However, in this case of hydrogenation of butanoic acid on Pd(111) surface, the computed activation barrier is very high of 181 kJ/mol (TS1-7, Fig. S19) and therefore is much less feasible than the Hydrogen-shuttling mechanism discussed in the previous section. However, once the complex intermediate is formed, the subsequent dehydroxylation from it is much easier with the low barrier of only 18 kJ/mol (TS2-7, Fig. S19), generating the butyraldehyde product which has the same carbon number as the butanoic acid feedstock.

4.6. Comparison between the activity of B5 vs F4 steps sites:

The model of p(4x8) with 4 missing rows on the top layer is used to evaluate the activity of Pd step sites. It is worth to mention that in this model, there are the presence of terrace site next to those step sites and is excellent representative for the 3 nm particle model. This model has more active sites and is therefore more appropriate than the use of periodic Pd(211) surface in literature. We have evaluated the activities of B5 steps site and F4 steps site for few reactions of butanoic acid and found that their activities are quite similar (Figure S20). Therefore, we only present the data observed at B5 step sites to discuss the activity of step sites in HDO reaction in the main text.

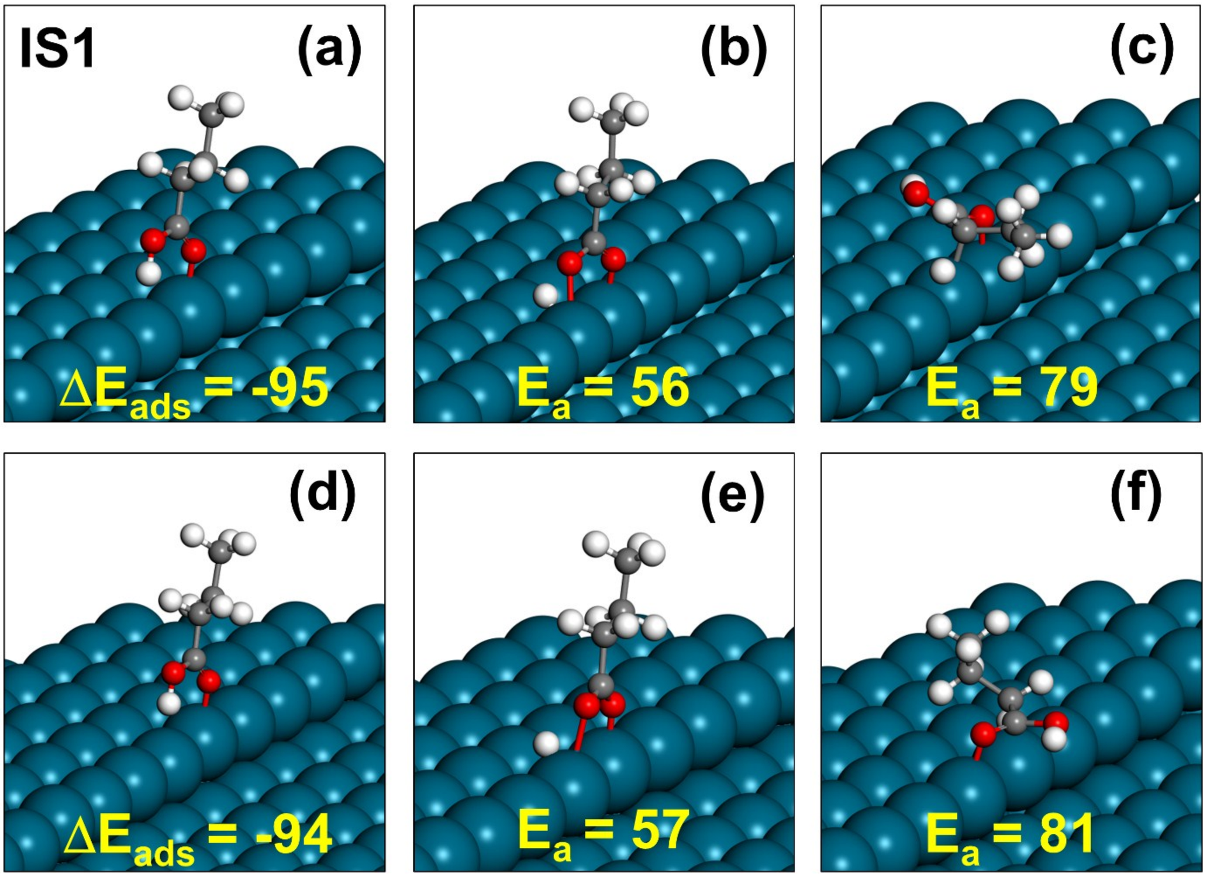

Figure S20. Activation of butanoic acid at B5 step sites: (a) Adsorption of butanoic acid at B5 step sites. (b) Initial O-H activation at B5 step sites. (c) Initial Cα-H activation at B5 step sites; Activation of butanoic acid at F4 step sites: (d) Adsorption of butanoic acid at F4 step sites. (b) Initial O-H activation at F4 step sites. (c) Initial Cα-H activation at F4 step sites;

4.7. Other competitive reactions along the DCX and DCN pathway for butanoic acid HDO conversion on step sites

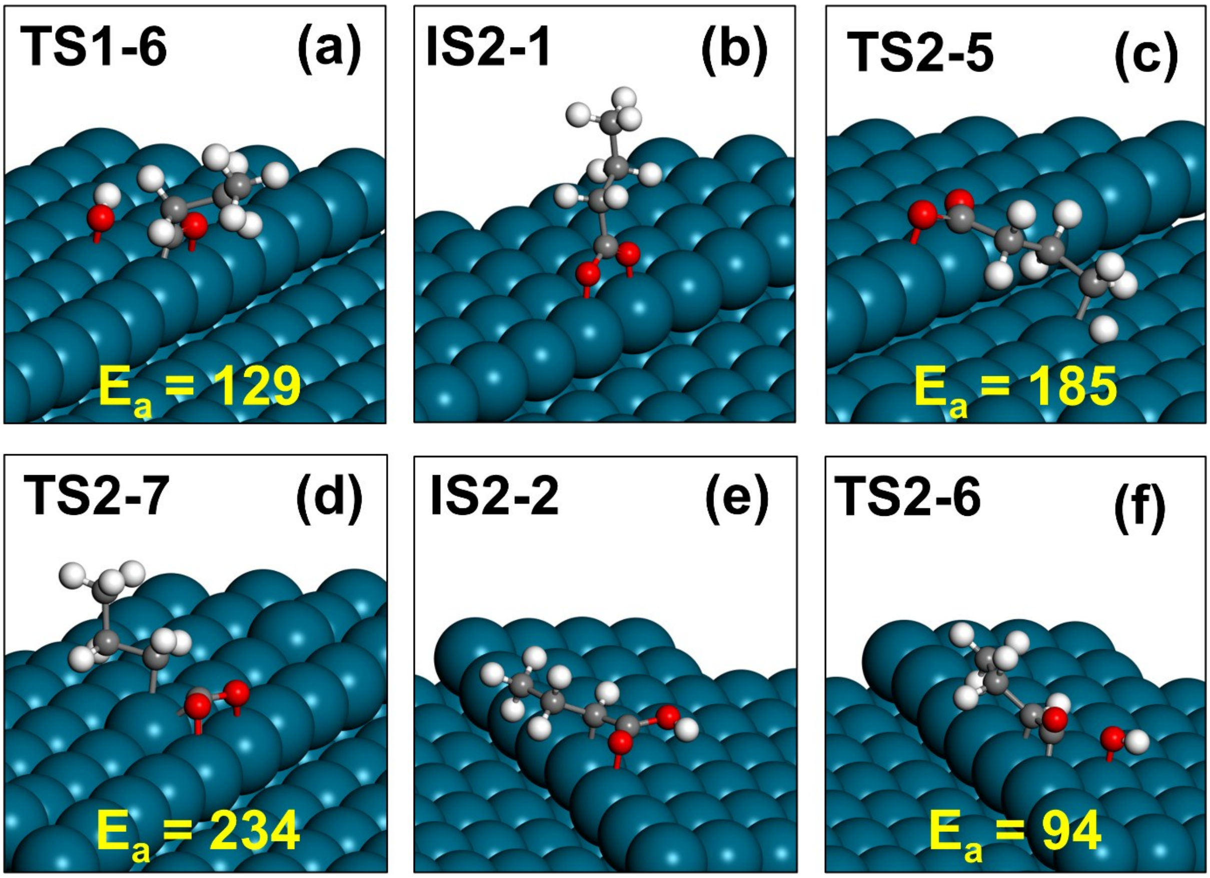

Figure S21. Reaction on Pd B5 step site: (a) Initial CO-OH scission from butanoic acid. (b) Adsorption of Butyrate at step sites. (c) C_γ-H activation on lower terrace sites from adsorbed Butyrate in step 2 of the DCX pathway. (d) Decarboxylation (-CO_2) from adsorbed Butyrate in step 2 of the DCX pathway. (e) Product of initial C_α-H activation from butanoic acid. (f) Subsequent CO-OH scission in step 2 of the DCN pathway.

4.8. Reactions along the RDO pathway on Pd B5 step sites

4.8.1. Hydrogen shuttling mechanism

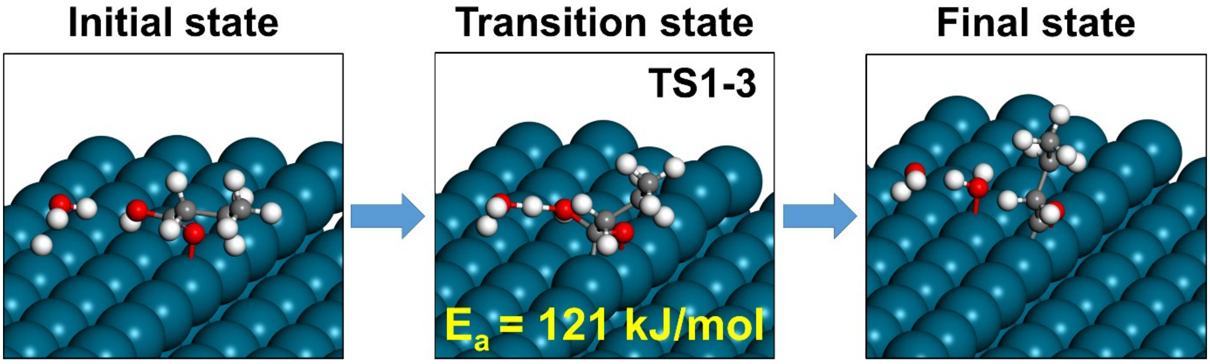

Figure S22. Initial state, Transition state and Final state for the Hydrogenation-dehydration reaction on Pd B5 step site via the Hydrogen-shuttling mechanism on Pd B5 step site

It could be seen that the Hydrogenation-dehydration reaction on Pd B5 step site via the Hydrogen-shuttling mechanism is not structural sensitive, and the barrier of this reaction on step site is only 5 kJ/mol lower than it is on terrace site. However, since the initial O-H activation from butanoic acid which triggers the DCN pathway is much stronger promoted on step site (barrier of only 79 kJ/mol), resulting in the higher preference of DCN pathway than RDO pathway for carboxylic acid HDO conversion on our Pd@PPN catalyst. It is excellently consistent with the high selectivity towards C17 alkane observed for the HDO of stearic acid on Pd@PPN catalyst presented in Table 1 of the main text.

4.8.2. Two-step Hydrogenation-dehydroxylation mechanism

Figure S23. Initial states, Transition states and Final states for the reactions along the two-step Hydrogenation-dehydroxylation mechanism on Pd B5 step site.

Surprisingly, the first step of hydrogenation into the butanoic acid forming a complex precursor for the dehydroxylation is strongly promoted on Pd B5 step site as shown in Figure S23, with the activation barrier of 135 kJ/mol (compare to 181 kJ/mol on Pd(111) terrace site). In the Initial state and transition state in Fig. S23, it could be seen that the H atom from subsurface position at Pd B5 step edge hydrogenates the butanoic acid to form the complex intermediate. It was also confirmed by pulsed molecular beam experiments that low-coordinated sites on Pd particles (step sites) play a crucial role in facilitating subsurface hydrogen diffusion at step sites.[55] As was reported in literature, the activity of subsurface Hydrogen in Pd is much stronger than the activity of on-surface Hydrogen,[55-57] explaining the strong promotional effect of step site for the hydrogenation into the butanoic acid. The subsequent dehydroxylation from this complex intermediate on Pd B5 step site is still very feasible (shown in Figure S24), although the activation barrier of 25 kJ/mol on B5 step site is slightly higher than it on terrace Pd(111) site (18 kJ/mol, Fig. S19).

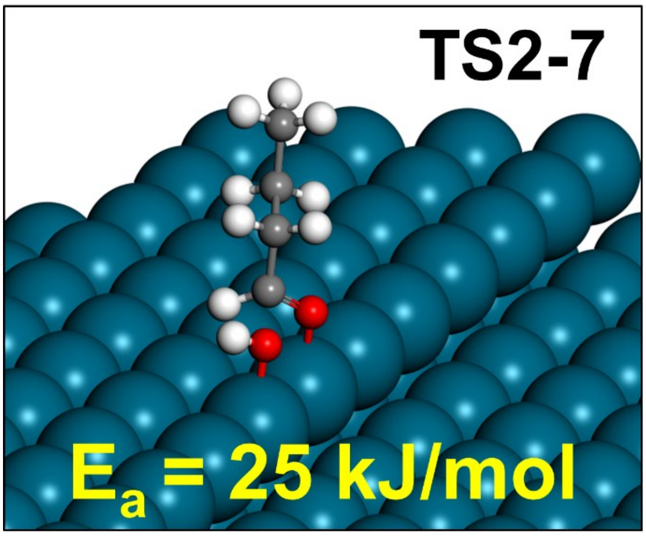

Figure S24. Transition state and activation barrier for the dehydrogenation of the complex intermediate in step 2 along the two-step Hydrogenation-dehydroxylation mechanism on Pd B5 step site.

REFERENCES

1. J. Mondal, Q. T. Trinh, A. Jana, W. K. H. Ng, P. Borah, H. Hirao and Y. Zhao, *ACS Applied Materials & Interfaces*, 2016, **8**, 15307-15319.
2. G. Xu, Y. Zhang, Y. Fu and Q. Guo, *ACS Catalysis*, 2017, **7**, 1158-1169.
3. M. J. Frisch, G. W. Trucks, H. B. Schlegel, G. E. Scuseria, M. A. Robb, J. R. Cheeseman, G. Scalmani, V. Barone, G. A. Petersson, H. Nakatsuji, X. Li, M. Caricato, A. V. Marenich, J. Bloino, B. G. Janesko, R. Gomperts, B. Mennucci, H. P. Hratchian, J. V. Ortiz, A. F. Izmaylov, J. L. Sonnenberg, Williams, F. Ding, F. Lipparini, F. Egidi, J. Goings, B. Peng, A. Petrone, T. Henderson, D. Ranasinghe, V. G. Zakrzewski, J. Gao, N. Rega, G. Zheng, W. Liang, M. Hada, M. Ehara, K. Toyota, R. Fukuda, J. Hasegawa, M. Ishida, T. Nakajima, Y. Honda, O. Kitao, H. Nakai, T. Vreven, K. Throssell, J. A. Montgomery Jr., J. E. Peralta, F. Ogliaro, M. J. Bearpark, J. J. Heyd, E. N. Brothers, K. N. Kudin, V. N. Staroverov, T. A. Keith, R. Kobayashi, J. Normand, K. Raghavachari, A. P. Rendell, J. C. Burant, S. S. Iyengar, J. Tomasi, M. Cossi, J. M. Millam, M. Klene, C. Adamo, R. Cammi, J. W. Ochterski, R. L. Martin, K. Morokuma, O. Farkas, J. B. Foresman and D. J. Fox, *Gaussian 16 Rev. A. 03.* Gaussian, Inc. Wallingford, CT, USA, 2016.
4. A. D. Becke, *Physical Review A*, 1988, **38**, 3098-3100.
5. C. Lee, W. Yang and R. G. Parr, *Physical Review B*, 1988, **37**, 785-789.
6. P. J. Hay and W. R. Wadt, *The Journal of Chemical Physics*, 1985, **82**, 299-310.
7. S. Grimme, *WIREs Computational Molecular Science*, 2011, **1**, 211-228.
8. V. Bertani, C. Cavallotti, M. Masi and S. Carrà, *The Journal of Physical Chemistry A*, 2000, **104**, 11390-11397.
9. G. Zanti and D. Peeters, *European Journal of Inorganic Chemistry*, 2009, **2009**, 3904-3911.
10. X. Xing, A. Hermann, X. Kuang, M. Ju, C. Lu, Y. Jin, X. Xia and G. Maroulis, *Scientific Reports*, 2016, **6**, 19656.
11. J. Rogan, G. García, M. Ramírez, V. Muñoz, J. Alejandro Valdivia, X. Andrade, R. Ramírez and M. Kiwi, *Nanotechnology*, 2008, **19**, 205701.
12. P. Nava, M. Sierka and R. Ahlrichs, *Physical Chemistry Chemical Physics*, 2003, **5**, 3372-3381.
13. E. D. Glendening, C. R. Landis and F. Weinhold, *Wiley Interdisciplinary Reviews: Computational Molecular Science*, 2012, **2**, 1-42.
14. J. Klimeš, D. R. Bowler and A. Michaelides, *Journal of Physics: Condensed Matter*, 2009, **22**, 022201.
15. J. Klimeš, D. R. Bowler and A. Michaelides, *Physical Review B*, 2011, **83**, 195131.
16. W. Liu, J. Carrasco, B. Santra, A. Michaelides, M. Scheffler and A. Tkatchenko, *Physical Review B*, 2012, **86**, 245405.
17. H. Yildirim, T. Greber and A. Kara, *The Journal of Physical Chemistry C*, 2013, **117**, 20572-20583.

18. J. Carrasco, W. Liu, A. Michaelides and A. Tkatchenko, *The Journal of Chemical Physics*, 2014, **140**, 084704.
19. Q. T. Trinh, A. V. Nguyen, D. C. Huynh, T. H. Pham and S. H. Mushrif, *Catalysis Science & Technology*, 2016, **6**, 5871-5883.
20. H. Yildirim and A. Kara, *The Journal of Physical Chemistry C*, 2013, **117**, 2893-2902.
21. C. T. Campbell, *Accounts of Chemical Research*, 2019, **52**, 984-993.
22. S. J. Carey, W. Zhao and C. T. Campbell, *Surface Science*, 2018, **676**, 9-16.
23. W. Zhao, S. J. Carey, S. E. Morgan and C. T. Campbell, *Journal of Catalysis*, 2017, **352**, 300-304.
24. T. L. Silbaugh, E. M. Karp and C. T. Campbell, *Journal of the American Chemical Society*, 2014, **136**, 3964-3971.
25. Y. Shiozawa, T. Koitaya, K. Mukai, S. Yoshimoto and J. Yoshinobu, *The Journal of Chemical Physics*, 2015, **143**, 234707.
26. K. Honkala, A. Hellman, I. N. Remediakis, A. Logadottir, A. Carlsson, S. Dahl, C. H. Christensen and J. K. Nørskov, *Science*, 2005, **307**, 555-558.
27. L. Zhou, J. M. P. Martirez, J. Finzel, C. Zhang, D. F. Swearer, S. Tian, H. Robatjazi, M. Lou, L. Dong, L. Henderson, P. Christopher, E. A. Carter, P. Nordlander and N. J. Halas, *Nature Energy*, 2020, **5**, 61-70.
28. J. Scaranto and M. Mavrikakis, *Surface Science*, 2016, **650**, 111-120.
29. J. K. Nørskov, F. Studt, F. Abild-Pedersen and T. Bligaard, in *Fundamental Concepts in Heterogeneous Catalysis*, eds. J. K. Nørskov, F. Studt, F. Abild-Pedersen and T. Bligaard, John Wiley & Sons, Inc., 2014, pp. 47-67.
30. Q. T. Trinh, A. Banerjee, Y. Yang and S. H. Mushrif, *The Journal of Physical Chemistry C*, 2017, **121**, 1099-1112.
31. R. W. Gosselink, S. A. W. Hollak, S.-W. Chang, J. van Haveren, K. P. de Jong, J. H. Bitter and D. S. van Es, *ChemSusChem*, 2013, **6**, 1576-1594.
32. J. Lu, S. Behtash, M. Faheem and A. Heyden, *Journal of Catalysis*, 2013, **305**, 56-66.
33. Y. K. Lugo-José, S. Behtash, M. Nicholson, J. R. Monnier, A. Heyden and C. T. Williams, *Journal of Molecular Catalysis A: Chemical*, 2015, **406**, 85-93.
34. J. Lu, S. Behtash and A. Heyden, *The Journal of Physical Chemistry C*, 2012, **116**, 14328-14341.
35. I. L. Simakova, O. A. Simakova, A. V. Romanenko and D. Y. Murzin, *Industrial & Engineering Chemistry Research*, 2008, **47**, 7219-7225.
36. S. Lestari, P. Mäki-Arvela, I. Simakova, J. Beltramini, G. Q. M. Lu and D. Y. Murzin, *Catalysis Letters*, 2009, **130**, 48-51.
37. L. Boda, G. Onyestyák, H. Solt, F. Lónyi, J. Valyon and A. Thernesz, *Applied Catalysis A: General*, 2010, **374**, 158-169.
38. J. P. Ford, J. G. Immer and H. H. Lamb, *Topics in Catalysis*, 2012, **55**, 175-184.
39. W. Jin, L. Pastor-Pérez, D. Shen, A. Sepúlveda-Escribano, S. Gu and T. Ramirez Reina, *ChemCatChem*, 2019, **11**, 924-960.

40. S. Kim, E. E. Kwon, Y. T. Kim, S. Jung, H. J. Kim, G. W. Huber and J. Lee, *Green Chemistry*, 2019, **21**, 3715-3743.

41. Q. Bu, H. Lei, A. H. Zacher, L. Wang, S. Ren, J. Liang, Y. Wei, Y. Liu, J. Tang, Q. Zhang and R. Ruan, *Bioresource Technology*, 2012, **124**, 470-477.

42. M. Snåre, I. Kubičková, P. Mäki-Arvela, D. Chichova, K. Eränen and D. Y. Murzin, *Fuel*, 2008, **87**, 933-945.

43. J. Dupont, P. A. Z. Suarez, M. R. Meneghetti and S. M. P. Meneghetti, *Energy & Environmental Science*, 2009, **2**, 1258-1265.

44. S. Lestari, P. Mäki-Arvela, H. Bernas, O. Simakova, R. Sjöholm, J. Beltramini, G. Q. M. Lu, J. Myllyoja, I. Simakova and D. Y. Murzin, *Energy & Fuels*, 2009, **23**, 3842-3845.

45. S. Lestari , P. Mäki-Arvela, J. Beltramini, G. Q. M. Lu and D. Y. Murzin, *ChemSusChem*, 2009, **2**, 1109-1119.

46. S. N. Naik, V. V. Goud, P. K. Rout and A. K. Dalai, *Renewable and Sustainable Energy Reviews*, 2010, **14**, 578-597.

47. N. Taufiqurrahmi and S. Bhatia, *Energy & Environmental Science*, 2011, **4**, 1087-1112.

48. D. D. Hibbitts, B. T. Loveless, M. Neurock and E. Iglesia, *Angewandte Chemie International Edition*, 2013, **52**, 12273-12278.

49. G. T. K. K. Gunasooriya, A. P. van Bavel, H. P. C. E. Kuipers and M. Saeys, *ACS Catalysis*, 2016, **6**, 3660-3664.

50. P. N. Amaniampong, Q. T. Trinh, B. Wang, A. Borgna, Y. Yang and S. H. Mushrif, *Angewandte Chemie International Edition*, 2015, **54**, 8928-8933.

51. P. N. Amaniampong, Q. T. Trinh, K. De Oliveira Vigier, D. Q. Dao, N. H. Tran, Y. Wang, M. P. Sherburne and F. Jérôme, *Journal of the American Chemical Society*, 2019, **141**, 14772-14779.

52. B. N. Zope, D. D. Hibbitts, M. Neurock and R. J. Davis, *Science*, 2010, **330**, 74-78.

53. M. S. Ide, B. Hao, M. Neurock and R. J. Davis, *ACS Catalysis*, 2012, **2**, 671-683.

54. P. N. Amaniampong, Q. T. Trinh, J. J. Varghese, R. Behling, S. Valange, S. H. Mushrif and F. Jérôme, *Green Chemistry*, 2018, **20**, 2730-2741.

55. W. Ludwig, A. Savara, R. J. Madix, S. Schauermann and H.-J. Freund, *The Journal of Physical Chemistry C*, 2012, **116**, 3539-3544.

56. D. Teschner, J. Borsodi, A. Wootsch, Z. Révay, M. Hävecker, A. Knop-Gericke, S. D. Jackson and R. Schlögl, *Science*, 2008, **320**, 86-89.

57. J. J. Velasco-Vélez, D. Teschner, F. Girgsdies, M. Hävecker, V. Streibel, M. G. Willinger, J. Cao, M. Lamoth, E. Frei, R. Wang, A. Centeno, A. Zurutuza, S. Hofmann, R. Schlögl and A. Knop-Gericke, *Topics in Catalysis*, 2018, **61**, 2052-2061.